Gabriel Kocher
kocherg0@etu.unige.ch

Dissipative Dynamics of Bosons in an Optical Lattice

Université de Genève (UNIGE)
Département de Physique Théorique

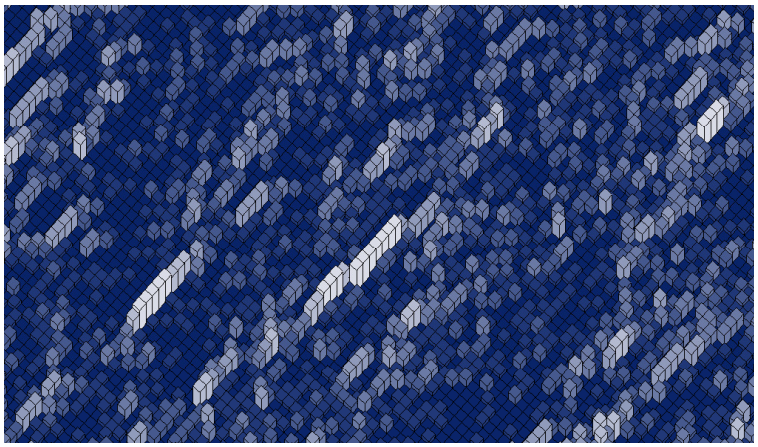

Under the supervision of:

Prof. Corinna Kollath
corinna.kollath@unige.ch

Expert:

Dr. Christophe Berthod
christophe.berthod@unige.ch

March 25, 2013

Contents

1 Introduction **4**

2 Bosonic atoms in optical lattices **5**
2.1 Bosonic quantum gases . . . 5
2.2 The Bose-Hubbard model . . . 6
2.2.1 Single particle in a periodic potential . . . 6
2.2.2 Derivation of the Bose-Hubbard model . . . 6
2.2.3 Phase diagram . . . 7
2.3 Dissipation model . . . 8
2.4 Weak coupling . . . 9
2.5 Physical link to spontaneous emission . . . 10

3 From quantum many-body to classical master equation **12**
3.1 Steady state . . . 13
3.2 Adiabatic elimination . . . 15

4 Normal diffusion **17**
4.1 Discrete random walk . . . 17
4.2 Continuous limit: Wiener process . . . 18

5 Anomalous diffusion, analytics **19**
5.1 Decoupling the equations . . . 19
5.1.1 Short term evolution . . . 20
5.2 Continuum description . . . 21
5.2.1 Sub-diffusive regime . . . 21
5.2.2 Long time evolution . . . 23

6 The Monte-Carlo algorithm **24**
6.1 Rejection-prone algorithm . . . 25
6.2 Rejection-free algorithm . . . 26
6.3 Observables, error estimation . . . 29

7 Anomalous diffusion: Monte-Carlo results, two sites **32**
7.1 Outline of analytical results . . . 32
7.2 Comparison to Monte-Carlo simulations . . . 33

8 Anomalous diffusion: Monte-Carlo results, L sites **35**
8.1 L sites: Summary of observables under study, and system parameters . . . 35
8.2 Overview . . . 37
8.3 Short-time regime . . . 37
8.4 Sub-diffusive regime . . . 40
8.5 Long term relaxation: finite systems at U=5 . . . 42
8.6 Long term relaxation: low filling, weakly interacting limit f=1, U=1 . . . 47
8.7 Long term relaxation: effect of interactions in the low filling limit f=1 . . . 49
8.8 Long term relaxation: effect of interactions in a system with high filling f=10 . . . 51

9 Summary and outlook **52**

Appendices **53**

Appendix A Exact fit parameters, long term relaxation **53**

Appendix B About the code **54**

CHAPTER 1

Introduction

In the development of quantum-based technologies, understanding the influence of the environment on a system is of capital importance. While high-precision clocks, measuring devices or quantum computers are developed, methods need to be elaborated to control and suppress the destruction of quantum coherence, induced by the surroundings.
In the study of quantum many body systems, cold atomic systems prove to be an ideal test-bed to understand environmental coupling: in the last decades, experimentalists have made stunning progress in the construction of highly tunable quantum emulators, where cooled atomic gases trapped in laser potentials can mimic predefined Hamiltonians. In such systems, heating processes appear in experiments for example via laser fluctuations, which give rise to noise on the lattice potential, or through collisional losses of atoms. The former have been theoretically studied recently [1], but experimentally the dominant heating mechanism is believed to be the incoherent scattering of the lattice photons and the resulting spontaneous emission of the trapped atoms [2]. For large interaction energies, several aspects of this problem have been studied in the first regime of decoherence [3], as well as on longer time scales, for two sites in [4] and [5], and for an infinite lattice in [6].
On the long term, the interplay between interaction and dissipation triggers a range of intriguing phenomena: while dissipation and interactions generally suppress coherence in the system, their joint action for example slow down the decoherence. Several dynamical diffusion regimes also appear, where the competition between interaction energy and heating processes makes way for non-Brownian motion and unconventional relaxation dynamics.
In this work we apply a Monte-Carlo technique to such a many atom system undergoing dissipative dynamics due to spontaneous emission of photons. An adiabatic elimination technique allows us to reduce the quantum problem to a stochastic many particle walk with anomalous diffusion factors. We address the short, medium and long term dynamics of the system beyond the decoherence timescale, with a direct comparison to analytical predictions. In this study, Monte Carlo sampling allows us to go beyond the current mean-field understanding of this problem.
We will start by introducing the models used to describe the bosonic system and the heating due to the environment (chap. 2), before describing the adiabatic elimination approach (chap. 3). We will then outline some analytical calculations both for random walks with normal (chap. 4) and anomalous diffusion factors (chap. 5), before introducing the Monte-Carlo algorithm (chap. 6). In the last chapters (chap. 7 and 8) we will present numerical results, and the resulting physical insight gained about the system.

CHAPTER 2

Bosonic atoms in optical lattices

2.1 Bosonic quantum gases

The realization of Bose-Einstein condensation in dilute atomic gases in 1995 [7, 8] has allowed to study fundamental quantum properties of macroscopic systems. Starting from an alkali gas at room temperature, a Bose Einstein condensate (BEC) is achieved by trapping, laser cooling and evaporative cooling of the atoms (see [9, 10]). In the resulting system, very low temperatures (in the micro-Kelvin regime) wash away 'classical' effects, leading the way to quantum degeneracy. At such low temperatures, a cloud of bosonic atoms enters a BEC phase were all atoms are in the lowest energy state. Manifestations of Bose-Einstein condensation have earlier been observed in more complicated systems (like the condensation of paired electrons in superconductors or Helium suprafluidity), but dilute atomic systems have proved to be unique systems, where experimentalists have an unprecedented level of control on the quantum gas.
Very interesting physics arises when a periodic lattice structure is given to the condensate. Formally, the obtained systems can mimic a number of condensed matter systems, with the advantage of being extremely versatile. Experimentally, once a BEC is formed, it is loaded onto an optical lattice, where a standing laser field creates potential barriers, proportional to the light intensity. Depending whether this external field is red-/blue-detuned compared to an atom's given resonating frequency, the AC-Stark shift creates spatial areas where atoms are attracted to/repelled from. In one dimension a typical potential is of the form: $V(x) = V_0 \cos^2(kx)$, where k is the laser wavenumber (related to the wavelength λ via $k = 2\pi/\lambda$). V_0 depends on the sign and on the amplitude of the detuning, as well as on the light intensity. Creating generic lattice configurations (in 1, 2, or 3 dimensions) boils down to finding an appropriate laser setup, and the resulting potential depth can easily be tuned.
In neutral atomic quantum gases, interactions are usually accounted for with point interactions $V_{\text{int}}(x-x') = \frac{4\pi a_s \hbar^2}{m}\delta(x-x')$, where a_s is the scattering length of the atom, and m its mass. In general boson experiments, highly correlated many-body systems [11] can be created with an appropriate choice of atom and wavelength. Among the prominent realizations with bosons we can for example cite the observations of quantum phase transitions like the superfluid to Mott-insulating state, which we will describe in the next section. In some cases, an external magnetic field allows a_s to be tuned over a wide range of values (Feshbach resonances).
We will first briefly introduce one of the prime models used to describe interacting bosons in a lattice: the Bose-Hubbard model. We will then outline a theoretical approach and physical interpretation of how dissipation can be added in such a system.

2.2 The Bose-Hubbard model

2.2.1 Single particle in a periodic potential

We first consider the single particle in a periodic potential problem [12]. The dynamics are governed by Hamiltonian $H_{1\text{part}} = \frac{p^2}{2m} + V_0(x)$, where m is the particle's mass, p its momentum and $V_0(x)$ the periodic lattice potential. The wave function of such a particle can be written as $\phi_q^{(n)}(x) = e^{iqx}u_q^{(n)}(x)$, where q is the particle's quasi-momentum (the Bloch wave number), and $u_q^{(n)}(x)$ is a function with the same periodicity as the lattice (it is called the Bloch eigenstate). With this ansatz, finding the stationary states can be written as the following eigenvalue problem :

$$H_q u_q^{(n)}(x) = E_q^{(n)} u_q^{(n)}(x) \tag{2.1}$$

where (n) indexes the eigenvalues $E_q^{(n)}$ of $H_q = \frac{(p+q)^2}{2m} + V_0(x)$. Fig. 2.1 plots the first few eigenvalues in the first Brillouin zone $q \in [-\hbar k, \hbar k]$, for a sinusoidal potential ($V(x) = V_0 \cos^2(kx)$). As a function of q, the eigenvalue spectrum is quadratic for $V_0 = 0$. This corresponds to the free particle dispersion, back-folded onto the first Brillouin zone (BZ). As the potential depth is increased, we first note a splitting of the levels on the edge of the BZ, followed by a flattening out of the bands. This leads to finite intra-band gaps.

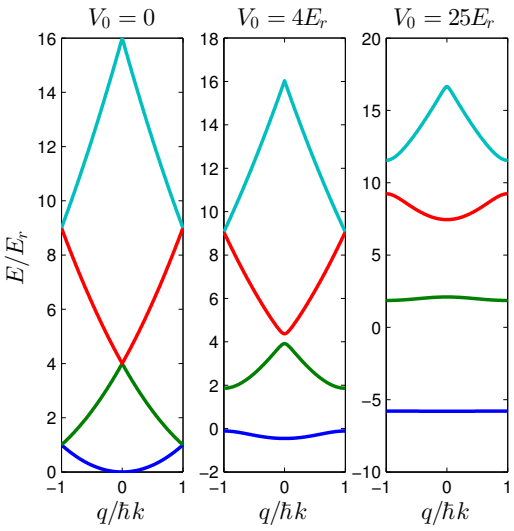

Figure 2.1: Plot of the first four energy bands in the Bloch spectrum, for increasing values of the potential depth. Energies are shown in terms of the recoil energy $E_r = \frac{(\hbar k)^2}{2m}$, where k is the laser wave number, and m the particle mass.

To describe interacting particles trapped in deep potentials, a more convenient single particle basis is a set of localized orthonormal wave functions, the Wannier functions: $w_n(x - x_i) = \mathcal{N}^{-1/2} \sum_q e^{-iqx_i} \phi_q^{(n)}(x)$. As the potential depth is increased, these functions become highly localized around the potential minima x_i, and are indexed by the band number n. The Wannier function in the lowest band for the sinusoidal potential is shown in fig.2.2(a,b) for a given potential depth. We note that this function tends towards a gaussian (it becomes exponentially localized) in the infinite barrier height limit, but that it generally has a wider tail.

2.2.2 Derivation of the Bose-Hubbard model

In second quantized language, the full Hamiltonian of an interacting many-particle system in a periodic potential is [13]:

$$H_{\text{full}} = \int \mathrm{d}x \left(\psi^\dagger(x) \left(\frac{p^2}{2m} + V_0(x) \right) \psi(x) + \frac{g}{2} \int dx \psi^\dagger(x)\psi^\dagger(x)\psi(x)\psi(x) \right) \tag{2.2}$$

Where $\psi(x)$ is the bosonic field operator for the atoms, and $g = \frac{4\pi a_s \hbar^2}{m}$.
In the limit where atomic interaction energies and thermal energies are smaller than the first Bloch band energy gap, a Wannier function expansion can be done. For deep lattices, we truncate to the lowest Bloch band Wannier function: $\psi(x) = \sum_i b_i w^{(0)}(x - x_i)$, where b_i is the destruction operator for a particle in the lowest band on site x_i. This yields the following hamiltonian:

$$H^{(0)} = -\sum_{i,j} J_{ij} b_i^\dagger b_j + \frac{1}{2} \sum_{i,j,k,l} U_{ijkl} b_i^\dagger b_j^\dagger b_k b_l \tag{2.3}$$

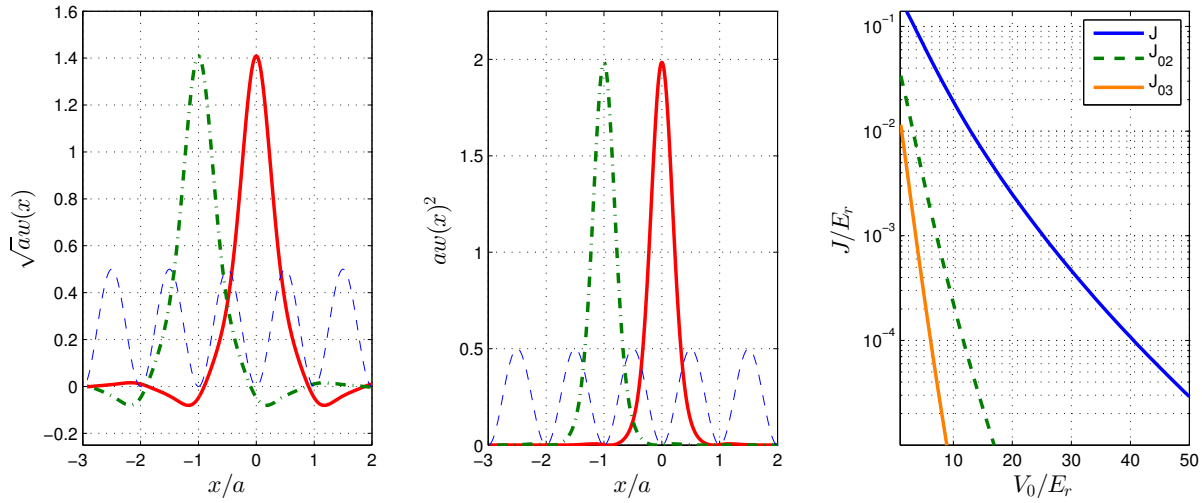

(a) (b) (c)

Figure 2.2: (a) The real part and (b) the modulus squared of the lowest band Wannier function at $x_i = 0$ (red) and $x_i = -1$ (green), for $V_0 = 3E_r$. The potential shape (blue dashed) is also shown. (c) The tunneling amplitude for a particle to its next, second next and third next neighbors (J, J_{02}, and J_{03}) as a function of the trapping potential amplitude. These are essentially determined by the overlap of the Wannier functions on neighboring sites, and become suppressed as the potential barrier is increased.

where we have written

$$J_{ij} = -\int \mathrm{d}x\; w_0(x - x_i)\left(\frac{p^2}{2m} + V_0(x)\right) w_0(x - x_j) \tag{2.4}$$

$$U_{ijkl} = g\int \mathrm{d}x\; w_0(x - x_i)w_0(x - x_j)w_0(x - x_k)w_0(x - x_l) \tag{2.5}$$

The J_{ij} factors are the hopping amplitude from site i to j. Computing the hopping amplitudes for several distances shows that the main contribution comes from nearest neighbors, while hopping to farther distances is suppressed by several orders of magnitude as the potential depth is increased (see fig.2.2(c)). A similar observation can be done for the U_{ijkl} factors which are the interaction matrix of particles on sites i, j, k, l: the biggest contribution comes from on-site interactions, i.e. all operators on the same site. Restricting to the dominant factors $J = J_{01}$ and $U = U_{0000}$ leads to the standard formulation of the Bose-Hubbard model (the J_{00} term has a constant contribution, which can be compensated by a chemical potential):

$$H = -J\sum_{l=1}^{L-1}\left(b_l^\dagger b_{l+1} + h.c.\right) + \frac{U}{2}\sum_{l=1}^{L} n_l\left(n_l - 1\right) \tag{2.6}$$

The operators b_l and b_l are bosonic creation and annihilation operators on site l and $n_l = b_l^\dagger b_l$ counts the number of atoms on site l. The tunneling matrix element $-J < 0$ describes the particle's ability to hop to a neighboring site, while the on-site repulsion $U > 0$ disfavors configurations with several particles on a single site.

2.2.3 Phase diagram

Although the Bose Hubbard model (2.6) is not exactly soluble (even in 1D, besides limiting cases), its phase diagram is rather well understood. The interplay between kinetic energy and on-site repulsion leads to the

superfluid-Mott insulator transition, which has been studied theoretically [14] and shown experimentally [15]. In the case $U \ll J$, the system is in a superfluid phase, and the ground state is given by a BEC wavefunction:

$$|SF\rangle = \left(\frac{1}{\sqrt{M}}\sum_j b_j^\dagger\right)^N |0\rangle \tag{2.7}$$

for a system with M sites and N particles, $|0\rangle$ being the vacuum state. The particle number fluctuations on site j are given by $\kappa = \langle SF|\, n_j^2\, |SF\rangle - \langle SF|\, n_j\, |SF\rangle^2 = \langle SF|\, n_j^2\, |SF\rangle - \left(\frac{N}{M}\right)^2 \approx \frac{N}{M}$, and stay finite for large systems. As the repulsive interaction strength is increased, if N/M is integer, a quantum phase transition to the Mott-insulating phase takes place, and the resulting ground state is characterized by an integer number of atoms per site and particle number fluctuations which tend to zero. In the $U \gg J$ limit, with an integer lattice filling $f = N/M$:

$$|MI\rangle \sim \prod_{i=1}^{M} (b_i^\dagger)^f\, |0\rangle \tag{2.8}$$

In this limit, moving a particle to a neighboring site costs an energy U, which means the ground state is insulating. The transition to the MI phase occurs on the boundary of the so-called 'Mott lobes' (see fig. 2.3). Starting from a superfluid state, a non integer N/M ratio can lead the system to maintain a superfluid state even in the $J \to 0$ limit (see fig. 2.3).

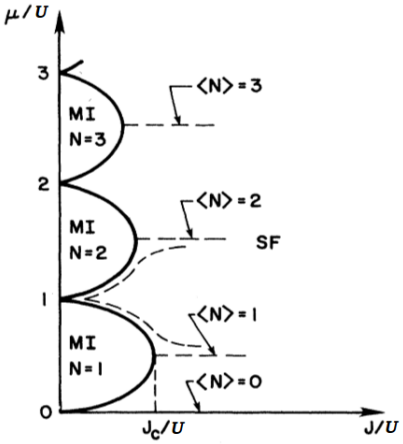

Figure 2.3: The Bose-Hubbard model's phase diagram $(\mu/U, J/U)$, where μ is the chemical potential (adapted from [14]). At high J/U ratios, a superfluid phase is present, while at low J/U ratios a Mott-insulating phase takes over. The MI phases are separated into Mott lobes, depending on the number of particles per site. For a non-integer number of atoms per site, the system maintains a superfluid state even in the $J \to 0$ limit (dashed trajectories between $\langle N\rangle = 1$ and $\langle N\rangle = 2$).

2.3 Dissipation model

In complete generality we suppose that our quantum system S is coupled to a bath B. The whole system follows the unitary dynamics of Hamiltonian H_{SB}:

$$H_{SB}(t) = H_S \otimes I_B + I_S \otimes H_B + H_I(t) \tag{2.9}$$

where $H_{S,B}$ are the self-Hamiltonians of the system and the bath, while $H_I(t)$ describes the interaction between them. In most situations the system environment can be considered as very large, and an accurate description of its infinite degrees of freedom reveals hopeless. Therefore, one tries to create an effective description of the restricted system S by taking an average over the irrelevant degrees of freedom of the bath:

$$\frac{d}{dt}\rho_S(t) = \mathrm{tr}_B \frac{d}{dt}\rho = -\frac{i}{\hbar}\mathrm{tr}_B[H_{SB}(t), \rho(t)] \tag{2.10}$$

where ρ and $\rho_S = \mathrm{tr}_B\rho$ are resp. the full and restricted system density matrices.
In this section, we will describe how, given certain assumptions, this equates to an extra term in the master equation of our bosonic system:

$$i\hbar\partial_t\rho_S = [H_S, \rho_S] + i\mathcal{D}\left(\rho_S\right) \tag{2.11}$$

The first term $[H_S, \rho_S]$ describes the unitary evolution of the density matrix ρ_S, while the second term accounts for the dissipation, and is of Lindblad form:

$$\mathcal{D}(\rho) = \Gamma \sum_{l=1}^{L} \frac{1}{2} [n_l, [n_l, \rho]] = \Gamma \sum_{l=1}^{L} \left(n_l \rho n_l - \frac{1}{2} n_l^2 \rho - \frac{1}{2} \rho n_l^2 \right) \tag{2.12}$$

where Γ is the coupling to the environment, and n_l the density operator on site l. There are several ways to understand this effective dissipation term, and we will briefly show 2 perspectives in the following sections.

2.4 Weak coupling

A first approach to dissipation comes from the theory of open quantum systems (see [16] chap. 3). Formally, assuming a weak coupling to the large bath, the dynamical eq. for ρ_S (2.10) can be cast into shape (2.11) via the definition of Lindblad operators containing the information about the exact nature of the coupling. This general approach outlines the semi-group structure in the generators behind the ρ_S evolution, but the general proof proves rather technical.
A part of this derivation can be done in a microscopic approach [17, 16]. Let us consider the density matrices in the interaction picture (in this representation we factor out the evolutions of the bath and the system):

$$\tilde{\rho}(t) = e^{i/\hbar(H_S+H_B)t} \rho(t) e^{-i/\hbar(H_S+H_B)t} \tag{2.13}$$

One can prove that:

$$i\hbar \dot{\tilde{\rho}} = [\tilde{H}_I, \tilde{\rho}] \tag{2.14}$$

where $\tilde{H}_I(t) = e^{i/\hbar(H_S+H_B)t} H_I e^{-i/\hbar(H_S+H_B)t}$. From (2.14) one deduces $\tilde{\rho}(t) = \tilde{\rho}(0) - i/\hbar \int \mathrm{d}t' \, [\tilde{H}_I(t'), \tilde{\rho}(t')]$, and replacing the solution back into (2.14) yields:

$$\dot{\tilde{\rho}}(t) = -\frac{1}{\hbar^2} \int \mathrm{d}t' \, \mathrm{tr}_B [\tilde{H}_I(t), [\tilde{H}_I(t'), \tilde{\rho}(t')]] + \frac{1}{i\hbar} [\tilde{H}_I(t), \tilde{\rho}(0)] \tag{2.15}$$

This expression is still completely general, but we now start considering approximations. Since $\mathrm{tr}_R(\tilde{\rho}) = \tilde{\rho}_S$, and assuming for simplicity that $\mathrm{tr}_B[\tilde{H}_I, \tilde{\rho}(0)]$, we can write:

$$\dot{\tilde{\rho}}_S(t) = -\frac{1}{\hbar^2} \int \mathrm{d}t' \, \mathrm{tr}_B [\tilde{H}_I(t), [\tilde{H}_I(t'), \tilde{\rho}(t')]] \tag{2.16}$$

This is where one applies a Born-Markov approximation: we assume the systems were initially decoupled, and that they maintain a small coupling, $\tilde{\rho}(t) \approx \tilde{\rho}_S(t) \tilde{\rho}_B(0)$ where $\tilde{\rho}_B(0)$ is a constant contribution (Born approximation). Additionally, assuming that $\dot{\tilde{\rho}}_S$ only depends on $\tilde{\rho}(t)$, rather than on its whole history $\tilde{\rho}(t')$ (Markov approximation), we arrive at the Redfield equation:

$$\dot{\tilde{\rho}}_S(t) = -\frac{1}{\hbar^2} \int \mathrm{d}t' \mathrm{tr}_B [\tilde{H}_I(t), [\tilde{H}_I(t'), \tilde{\rho}_S(t) \tilde{\rho}_B(0)]] \tag{2.17}$$

This equation resembles the Lindblad form. The exact (2.11) shape can be recovered, but operators describing the exact nature of the coupling need to be defined (the Lindblad operators).
This derivation points out the major approximations involved in extracting a Lindblad dissipator, and among these we should point out the markovian approach. In essence, the system S can depend on its past history only if its earlier states become imprinted with the evolution in the reservoir (evolution resulting from the $\tilde{H}_I$ term). If we, however, assume that the environment is kept in thermal equilibrium, we do not expect it to exhibit the minor changes influenced by S for a long time. In fact such correlations induced in the bath by S will decay extremely fast compared to the system timescale, so we can neglect them (coarse graining).

Sidenote: An interesting interpretation of the Lindblad dissipator is found when computing the effect of measurements on a quantum system. Say our quantum system is measured at every time interval θ. If one accounts for the unitary evolution of system S over intervals θ, and projects the system onto observable eigenstates periodically, one also recovers a term like (2.12). In this derivation one needs to assume that the canonically conjugated variable to the observable operator does not drift from measurement to measurement (this is an equivalent of the Markovian approx). In the $\theta \to 0$ limit, the system's evolution is frozen, which is a manifestation of the Quantum Zeno effect (see [16]). Note here that there are no constraints on θ, the weak coupling condition is not required to recover the Lindblad shape.

2.5 Physical link to spontaneous emission

Single particle picture: To understand the heating processes involved in (2.12), we start by outlining the heating mechanisms of single particles in optical lattices. A more complete description of these phenomena can be found in [18, 3]. The optical Bloch equations describe the interactions of an atom with a light field. These can be derived by assuming a dipole interaction, and by tracing out irrelevant degrees of freedom, assuming a Markovian evolution (see last section). As an illustration of the Lindblad operators, consider a two-level atom in the rotating (with the laser frequency) frame ($\hbar = 1$):

$$\dot{\rho} = -i[H, \rho] + \Gamma \int d^2\mathbf{u} N(\mathbf{u}) \left(C_{\mathbf{u}} \rho C_{\mathbf{u}}^\dagger - \frac{1}{2} \rho C_{\mathbf{u}}^\dagger C_{\mathbf{u}} - \frac{1}{2} C_{\mathbf{u}} C_{\mathbf{u}}^\dagger \rho \right) \tag{2.18}$$

with atomic Hamiltonian

$$H_{\text{2level}} = \frac{\mathbf{p}^2}{2m} - \Delta \left|e\right\rangle \left\langle e\right| - \left(\left|g\right\rangle \left\langle e\right| \frac{\Omega(\hat{\mathbf{x}})}{2} + h.c. \right) \tag{2.19}$$

Here $|g\rangle$ and $|e\rangle$ are the two levels of the atom described by the reduced density matrix ρ, and Γ is the decay rate of the excited state e. In the master equation we recognize the unitary evolution of the Hamiltonian, and the Lindblad operators $C_{\mathbf{u}} = |g\rangle \langle e| e^{-ik\mathbf{u}\cdot\hat{\mathbf{x}}}$ describe the relaxation to the ground state after a spontaneous photon emission in direction $\mathbf{u}$, as well as the corresponding recoil felt by the atom. k is the wave number associated with the concerned atomic transition, and $N(\mathbf{u})$ is the distribution of the emitted photons.
In Hamiltonian (2.19), the kinetic energy and atom interaction with the laser are accounted for. Δ is the laser's detuning with respect the atom's resonant frequency. The last term in (2.19) depends on the spatially dependent Rabi frequency, proportional to the atom's dipole moment and the intensity of the electric field.

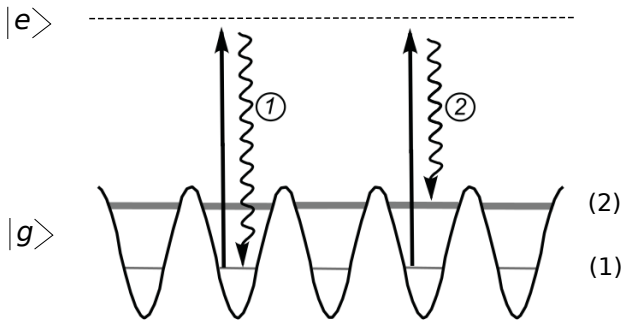

Figure 2.4: Two heating mechanisms arising from the interactions of an atom with a light field and with spontaneous emission. (1) and (2) are the two lowest Bloch bands of the lattice, while $|g\rangle$ and $|e\rangle$ are two atomic levels. Adapted from [18]

To understand the mechanisms arising in this description, we consider atoms trapped in the lowest Bloch band of the lattice ((1) in fig. 2.4), in their ground state ($|g\rangle$ in fig. 2.4). In principle, once interaction

occurs with the light field, the atom is excited (state $|e\rangle$ in fig. 2.4). It then quickly relaxes (by spontaneous emission) back to its ground state by emitting a photon into the environment (trajectory 1 in fig. 2.4). This fast relaxation is due to the fact that the excited atomic level is much more energetic than typical Bloch band gaps (the $|g\rangle$ to $|e\rangle$ transition is roughly 1000 THz, while the transition from (1) to (2) is typically 10-100 KHz in experiments). Assuming a large enough detuning $|\Delta| \ll \Omega$, the excited state can be adiabatically eliminated from the model (the evolution is coarse grained to only show long term evolution).
We should however note that if the Bloch band gap between the lowest and the first excited state is finite (large but not very large), this relaxation can also be done to state (2) (trajectory (2) in fig. 2.4). In this case, atoms landing in the (2) state usually decay to (1) over timescales much longer than typical experiments[1], and this would lead to atom losses in a description truncated to the lowest band. With high potential barriers, we would expect that this scenario is strongly suppressed, but a more in-depth analysis reveals that this is very dependent on the sign of the detuning. For a blue-detuned lattice (where the electric field repels atoms from potential maxima), ground state heating rates (trajectory (1)) tend to be suppressed as heating to higher bands is favored. It is only for red-detuned lattices (where the electric field attracts atoms to potential minima) that the ground state heating is understood as the dominant heating mechanism [18, 3]. Note that additionally to the large band gap and large detuning assumptions, scattering processes to neighboring sites are generally neglected due to the exponential localization of the Wannier functions.

N-particle picture: To upgrade this description to a many-particle model, there are several steps: Once a continuous model is established for N particles (using a continuous N-particle Hamiltonian like (2.2) but including several atomic levels, and adding laser interaction terms), the excited states need to be eliminated (adiabatic elimination), and the result needs to be expanded in Wannier basis. The resulting Fock-basis representation is then a Multi-Band Bose-Hubbard model (generalization of the Bose-Hubbard model to several Bloch bands) under dissipation. For red detuning, it is then possible (see last paragraph) to truncate the model to the lowest Bloch band, which yields the exact form (2.11) [3].

[1] This is not always clear. If the Bloch band gap is small, the decay from (2) to (1) can be very fast. Double occupancy of state (2) can for example lead one particle to relax to (1) and the other to excite to $|e\rangle$ in a rapid process.

CHAPTER 3

From quantum many-body to classical master equation

Following sections 2.2 and 2.3, the complete master equation of the bosonic system undergoing dissipation can be written as:

$$i\hbar\partial_t\rho = [H,\rho] + i\mathcal{D}(\rho) \qquad \text{(eq. 2.11)} \tag{3.1}$$

where the first term $[H,\rho]$ describes the unitary evolution of the density matrix (with hamiltonian (2.6)), while the second term accounts for the dissipation (with dissipator (2.12)).

To understand the dynamics of the system, we start by studying the steady state of the quantum problem (3.1), before setting up an approximate set of classical equations, that we will later use for numerical and analytical investigation.

To understand the asymptotic behavior of the system, we start by considering the effect of the dissipator on ρ. A general density matrix can be written as $\rho = \sum_{\mathbf{n},\mathbf{m}} \rho^{\mathbf{m}}_{\mathbf{n}} |\mathbf{n}\rangle\langle\mathbf{m}|$, where $|\mathbf{n}\rangle\langle\mathbf{m}|$ is a projection operator, and $\rho^{\mathbf{m}}_{\mathbf{n}}$ the corresponding matrix element. A state $|\mathbf{n}\rangle$ is a collection of L variables, corresponding to the atom number on each lattice site $|\mathbf{n}\rangle = |n_1, n_2, ..., n_L\rangle$.
We first notice that any diagonal density matrix $\rho_D = \sum_{\mathbf{n}} \rho^{\mathbf{n}}_{\mathbf{n}} |\mathbf{n}\rangle\langle\mathbf{n}|$ is in the dissipation free subspace, i.e. $\mathcal{D}(\rho_D) = 0$. Furthermore, the interaction term $\frac{U}{2}\sum_{l=1}^{L} n_l(n_l-1)$ is also diagonal in Fock basis. It follows that finding a steady state reduces to finding density matrix elements which cancel the tunneling term. More precisely, the diagonal elements of eq. (3.1) are:

$$\begin{aligned}
i\hbar\partial_t \rho^{\cdot,l,m,n,\cdot}_{\cdot,l,m,n,\cdot} &= \ldots \\
&- J\Big[\sqrt{(l+1)m}\left(\rho^{\cdot,l+1,m-1,n,\cdot}_{\cdot,l,m,n,\cdot} - \rho^{\cdot,l,m,n,\cdot}_{\cdot,l+1,m-1,n,\cdot}\right) \\
&+ \sqrt{(m+1)l}\left(\rho^{\cdot,l-1,m+1,n,\cdot}_{\cdot,l,m,n,\cdot} - \rho^{\cdot,l,m,n,\cdot}_{\cdot,l-1,m+1,n,\cdot}\right) \\
&+ \sqrt{(m+1)n}\left(\rho^{\cdot,l,m+1,n-1,\cdot}_{\cdot,l,m,n,\cdot} - \rho^{\cdot,l,m,n,\cdot}_{\cdot,l,m+1,n-1,\cdot}\right) \\
&+ \sqrt{(n+1)m}\left(\rho^{\cdot,l,m-1,n+1,\cdot}_{\cdot,l,m,n,\cdot} - \rho^{\cdot,l,m,n,\cdot}_{\cdot,l,m-1,n+1,\cdot}\right)\Big] \\
&+ \ldots
\end{aligned} \tag{3.2}$$

In this expression we note that the hopping factor J relates the dynamics of diagonal elements to first

off-diagonal elements. For the first off diagonals we get:

$$\begin{aligned} i\hbar\partial_t \rho^{\cdot,l+1,m-1,n,\cdot}_{\cdot,l,m,n,\cdot} &= [-i\Gamma + (l-m+1)U]\,\rho^{\cdot,l+1,m-1,n,\cdot}_{\cdot,l,m,n,\cdot} \\ &- J\sqrt{(l+1)m}\left(\rho^{\cdot,l,m,n,\cdot}_{\cdot,l,m,n,\cdot} - \rho^{\cdot,l+1,m-1,n,\cdot}_{\cdot,l+1,m-1,n,\cdot}\right) \end{aligned} \tag{3.3}$$

Here we note once more a how J relates diagonal to off-diagonal motion, while Γ and U affect only off-diagonal elements.

3.1 Steady state

Substituting ρ_D into eq. (3.2) reveals that all diagonal matrix elements need to be constants $\rho^{n_1,\dots,n_L}_{n_1,\dots,n_L} = C^{n_1,\dots,n_L}_{n_1,\dots,n_L}$ to ensure a steady state on the diagonal. On the other hand, substituting this result into eq. (3.3) shows that the only way to freeze the first off-diagonal motion is to set $C^{\cdot,l+1,m-1,n,\cdot}_{\cdot,l+1,m+1,n,\cdot} = C^{\cdot,l,m,n,\cdot}_{\cdot,l,m,n,\cdot}$.
Since all system configurations can be reached by a finite number of particle tunnelings, and that neighboring (that are reached by a 1 particle hop) density matrix elements can be related by an equation such as eq. (3.3), we can conclude that the unique steady state must have equal terms on the diagonal. It can be shown that given this assumption, all off diagonal motion vanishes, and the steady state is therefore:

$$\rho = \frac{\mathbb{1}}{M} \tag{3.4}$$

Where M is the dimension of the Hilbert space. In this maximal entropy state, all configurations are equally likely. The Hilbert space dimension is given by the number of possibilities to distribute N indistinguishable particles onto L sites, that we call $C(N,L) = M = \binom{N+L-1}{L-1} = \frac{(N+L-1)!}{(L-1)!N!}$.

To determine the asymptotic value of observables, we will however be more interested in the one- and two- site reduced density matrices. These are determined in a similar way, but tracing out all sites except resp. i or (i,j):

$$\rho^{(1)}_{n_i} = \mathrm{tr}_{\mathrm{sites}\neq i}\ \rho = \frac{C(N-n_i,L-1)}{C(N,L)} = \frac{(N-n_i+L-2)!(L-1)!N!}{(N-n_i)!(L-2)(N+L-1)!} \tag{3.5}$$

$$\rho^{(1)}_{n_i,n_j} = \mathrm{tr}_{\mathrm{sites}\neq i\neq j}\ \rho = \frac{C(N-n_i-n_j,L-2)}{C(N,L)} = \frac{(N-n_i-n_j+L-3)!(L-1)!N!}{(N-n_i-n_j)!(L-3)(N+L-1)!} \tag{3.6}$$

In following sections, $\rho^{(1)}_{n_i}$ will be referred to as the finite size asymptotic matrix element distribution (since we will only be looking at the 1-site reduced density matrix), and we will write it as ρ^L_n. Its $L\to\infty$ limit at fixed lattice filling $f = N/L$ will also be of interest:

$$\rho^L_n = \frac{(N-n_i+L-2)!(L-1)!N!}{(N-n_i)!(L-2)(N+L-1)!} \underset{L\to\infty}{\to} \rho^\infty_n = \frac{1}{f}\left(\frac{f}{1+f}\right)^{n+1}. \tag{3.7}$$

The finite chain and infinite chain ($L\to\infty$ limit at $f = N/L$ fixed) asymptotic expressions for resp. the average density, the local density fluctuations (compressibility) and the density-density correlations can be expressed by:

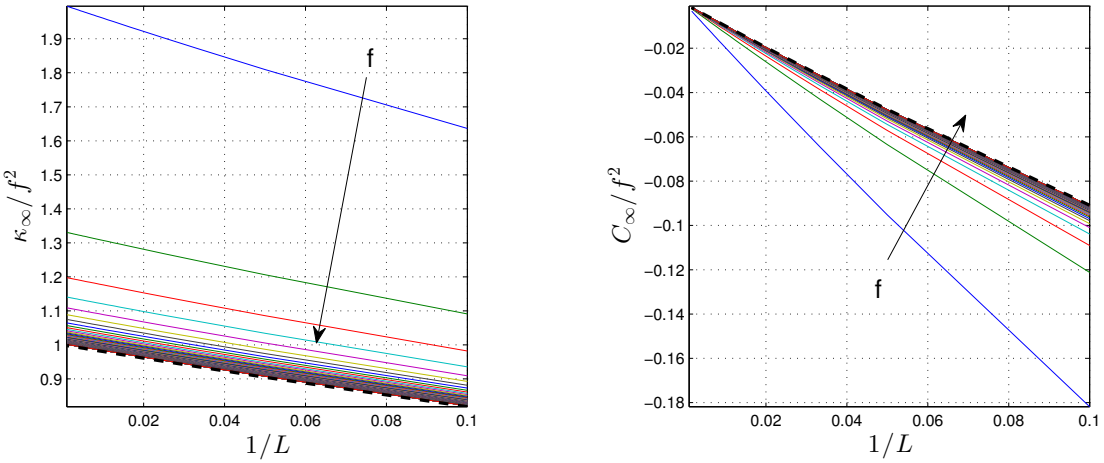

(a) (b)

Figure 3.1: Asymptotic value of the density fluctuations (a) and correlations (b) versus system length, for lattice fillings f=1-200 in integer spacing. The black dashed lines are the limits of $f \to \infty$. At large system sizes, the fluctuations converge towards a finite value, while the correlations vanish. For short systems, important finite size effects are to be expected.

$$\begin{aligned}
\langle n \rangle &= \sum_{n_1,\ldots,n_L=0}^{N} n_i \rho^{n_1,\ldots,n_L}_{n_1,\ldots,n_L} = \sum_{n_i=0}^{N} n \rho^{(1)}_{n,n} \\
&= \sum_{n_i=0}^{N} n \frac{C(N-n, L-1)}{C(N,L)} = \frac{N}{L} = f \qquad (3.8) \\
\kappa^L_\infty / f^2 &= \frac{\langle n_i^2 \rangle - \langle n_i \rangle^2}{f^2} = \sum_{n_i=0}^{N} (n_i/f)^2 \rho^{(1)}_{n,n} - 1 \\
&= \frac{(L-1)(L+N)}{(L+1)N} = \frac{(L-1)(1+f)}{(L+1)f} \underset{L\to\infty}{\to} \rho_\infty = \frac{1+f}{f} \qquad (3.9) \\
C^L_\infty(d)/f^2 &= \frac{\langle n_i n_{i+d} \rangle - \langle n_i \rangle^2}{f^2} = \sum_{n_i=0}^{N} \sum_{n_{i+d}=0}^{N-n_i} \frac{n_i n_{i+d}}{f^2} \rho^{(2)} - 1 \\
&= \frac{L(1-N)}{N(L+1)} - 1 = \frac{fL-1}{f(L+1)} - 1 \underset{L\to\infty}{\to} 0 \qquad (3.10)
\end{aligned}$$

The behavior of the C^L_∞ and the κ^L_∞ are plotted in fig.(3.1) versus $1/L$ for different fillings. For finite systems, both the fluctuations and the correlations have a non-zero value. The κ value decreases as the filling is increased, to converge towards 1 for infinite filling: $\lim_{f\to\infty} \kappa^L_\infty / f^2 = \frac{1-1/L}{1+1/L}$. On the other hand the correlations vanish only for infinite chains, and raising the filling only reduces the finite size effect slightly, $\lim_{f\to\infty} C^L_\infty / f^2 = \frac{1}{1+1/L} - 1$. Here we see that reaching the $L \to \infty$ steady state can only be hoped for in very large systems ($L \sim 1000$).
Notice that asymptotically the density correlation value does not depend on d. This means that in the asymptotic state, correlations either need to vanish (infinite system) or even out over the chain (finite system).

3.2 Adiabatic elimination

In the non-interacting limit $U \approx 0$, and assuming $\Gamma \gg J$ is the dominant parameter, the first time regime is characterized by decoherence: far off-diagonal terms of the density matrix will decay exponentially fast, and only terms close to the diagonal will contribute on a longer timescale. This can be understood using the off-diagonal dynamical equations. Considering only 1 site: $\langle n|\,\mathcal{D}(\hat{\rho})\,|n+d\rangle = -\frac{\Gamma}{2}d^2\rho_n^{n+d}$. This term dominates the off-diagonal differential eq. $i\hbar\partial_t\rho_{\cdot,l,m,n,\cdot}^{\cdot,l+d,m-d,n,\cdot} \propto -id^2\Gamma\rho_{\cdot,l,m,n,\cdot}^{\cdot,l+d,m-d,n,\cdot}$, which leads to a decay $\rho_{\cdot,l,m,n,\cdot}^{\cdot,l+d,m-d,n,\cdot} \propto e^{-\alpha d^2\Gamma t}$, where α is a constant.
When the interaction is added, off diagonal elements will however also be under the influence of a non negligible phase factor due to the interaction term in the Hamiltonian. At this point we resort to an adiabatic elimination technique (see [4, 5, 19, 20], and note that this can also be done for a fermionic system [21]), that will allow us to coarse grain the system's dynamics (eliminate the fast degrees of freedom): In the limit $U \gg J$ and $\Gamma \gg J$, off diagonal terms will be quickly evolving, decaying much faster than the diagonal terms. Their evolution can therefore be integrated out, leaving us with a set of equations valid at large enough times $t \gg (\Gamma/\hbar)^{-1}$. Care needs to be applied though: the system's slow diagonal evolution is governed by the hopping parameter J, connecting diagonal to first off diagonal terms. To accurately coarse grain the system's dynamics, their behavior needs to be incorporated.

A solution to eq. (3.3) can be written as

$$\begin{aligned}\rho_{\cdot,l,m,n,\cdot}^{\cdot,l+1,m-1,n,\cdot}(t) &= e^{-[\Gamma+i(l-m+1)U]t/\hbar}\rho_{\cdot,l,m,\cdot}^{\cdot,l+1,m-1,\cdot}(0) \\ &+ \frac{i}{\hbar}J\sqrt{(l+1)m}e^{-[\Gamma+i(l-m+1)U]t/\hbar}\int_0^t e^{[\Gamma+i(l-m+1)U]t'/\hbar}\left(\rho_{\cdot,l,m,\cdot}^{\cdot,l,m,\cdot}(t') - \rho_{\cdot,l+1,m-1,\cdot}^{\cdot,l+1,m-1,\cdot}(t')\right)dt'\end{aligned}$$

For $t \gg (\Gamma/\hbar)^{-1}$, the first term can be neglected, since it decays rapidly. The second term can be dealt with by integrating by parts: the integral term will contain derivatives of $\rho_{\cdot,l,m,\cdot}^{\cdot,l,m,\cdot}$ and $\rho_{\cdot,l+1,m-1,\cdot}^{\cdot,l+1,m-1,\cdot}$. These terms can be re-expressed with the master equation, but they will only produce terms containing a factor J which, combined with the J/U^2 prefactor of the integral produces only $O(J^2)$ terms. We choose to retain leading order terms in J, and we are left with the contents of the boundary term which yields:

$$\begin{aligned}\rho_{\cdot,l,m,n,\cdot}^{\cdot,l+1,m-1,n,\cdot}(t) &= \frac{J\sqrt{(l+1)m}}{(l-m+1)^2U^2+\Gamma^2}\left[(l-m+1)U+i\Gamma\right] \\ &\times \left(\rho_{\cdot,l,m,n,\cdot}^{\cdot,l,m,n,\cdot}(t) - \rho_{\cdot,l+1,m-1,n,\cdot}^{\cdot,l+1,m-1,n,\cdot}(t)\right)\end{aligned}$$

This result can then be substituted in eq. (3.2), and we obtain a master equation containing only diagonal density matrix terms:

$$\begin{aligned}\hbar\partial_t\rho_{\cdot,l,m,n,\cdot}^{\cdot,l,m,n,\cdot} &= \ldots \\ &- \frac{2J^2\Gamma(l+1)m}{(l-m+1)^2U^2+\Gamma^2}\left(\rho_{\cdot,l,m,n,\cdot}^{\cdot,l,m,n,\cdot} - \rho_{\cdot,l+1,m-1,n,\cdot}^{\cdot,l+1,m-1,n,\cdot}\right) \\ &- \frac{2J^2\Gamma(m+1)l}{(m-l+1)^2U^2+\Gamma^2}\left(\rho_{\cdot,l,m,n,\cdot}^{\cdot,l,m,n,\cdot} - \rho_{\cdot,l-1,m+1,n,\cdot}^{\cdot,l-1,m+1,n,\cdot}\right) \\ &- \frac{2J^2\Gamma(m+1)n}{(m-n+1)^2U^2+\Gamma^2}\left(\rho_{\cdot,l,m,n,\cdot}^{\cdot,l,m,n,\cdot} - \rho_{\cdot,l,m+1,n-1,\cdot}^{\cdot,l,m+1,n-1,\cdot}\right) \\ &- \frac{2J^2\Gamma(n+1)m}{(n-m+1)^2U^2+\Gamma^2}\left(\rho_{\cdot,l,m,n,\cdot}^{\cdot,l,m,n,\cdot} - \rho_{\cdot,l,m-1,n+1,\cdot}^{\cdot,l,m-1,n+1,\cdot}\right) \\ &- \ldots\end{aligned} \tag{3.11}$$

Which we then re-write as:

$$\begin{aligned}
\hbar\partial_t \rho^{.,l,m,n,.}_{.,l,m,n,.} &= ... \\
&- T(l,m)\left(\rho^{.,l,m,n,.}_{.,l,m,n,.} - \rho^{.,l+1,m-1,n,.}_{.,l+1,m-1,n,.}\right) \\
&- T(m,l)\left(\rho^{.,l,m,n,.}_{.,l,m,n,.} - \rho^{.,l-1,m+1,n,.}_{.,l-1,m+1,n,.}\right) \\
&- T(m,n)\left(\rho^{.,l,m,n,.}_{.,l,m,n,.} - \rho^{.,l,m+1,n-1,.}_{.,l,m+1,n-1,.}\right) \\
&- T(n,m)\left(\rho^{.,l,m,n,.}_{.,l,m,n,.} - \rho^{.,l,m-1,n+1,.}_{.,l,m-1,n+1,.}\right) \\
&- ...
\end{aligned} \tag{3.12}$$

with $T(m,n) = 2\left(\frac{J}{U}\right)^2 \Gamma \frac{(m+1)n}{(m-n+1)^2+(\Gamma/U)^2}$. Here we should notice that the total probability is conserved ($\partial_t \sum^*_{\mathbf{n}} \rho^{.,l,m,n,.}_{.,l,m,n,.} = 0$, where $\mathbf{n} = (..,l,m,n,..)$, and the sum is constrained by $\sum_i n_i = ...+l+m+n+... = N$). We can extract the rate for a particle to hop from a given site to a neighboring site: considering a starting site indexed by k, of population m and a target site of population n (left or right), the hopping rates to the left and right are given by the transition amplitudes between configurations $\{m,n\}$ to $\{m-1,n+1\}$ or $\{n,m\}$ to $\{n+1,m-1\}$:

$$W_{nm} = W_{\underset{\rightarrow}{k}} = W_{\underset{\leftarrow}{k}} = T(m-1,n+1) = 2\left(\frac{J}{U}\right)^2 \Gamma \frac{m(n+1)}{(m-n-1)^2+(\Gamma/U)^2} \tag{3.13}$$

At this point it is interesting to recall that our starting point was a complex quantum many-body system, exhibiting quantum phase transitions and correlations. In fact, if off-diagonal order existed in the initial density matrix, this order is destroyed on a $\Gamma/\hbar$ timescale, due to the heating process. This comes from the fact that spontaneous emission events localize the atoms undergoing the process, or that the information about the atom's position is transmitted to the environment via the emitted photon. As a result, we are left with a classical mixture of locations where the atoms could have scattered. Although there is still quantum coherence in the system, dissipation reduces the problem to a classical master equation (eq. (3.11)), interpreted as a stochastic walk with anomalous diffusion factors.

Formulated in this way, the dynamics of the system does not depend on the value chosen for J or Γ separately anymore. In eq. (3.13), the $2\left(J/U\right)^2\Gamma$ constant defines the timescale on which the system evolves, and the factor will be absorbed when we define a rescaled time τ (see sect. 5). As a result, the dynamics only depends on the Γ/U ratio. In the following, U will be expressed in units of Γ.
In sect. 5, under certain approximations, we will review some analytical expressions derived for the short, medium and long time behaviors of the system. In sect. 6 we describe how we approach the full lattice problem using Monte-Carlo sampling.

CHAPTER 4

Normal diffusion

Before analytically tackling our dissipative bosonic problem, it appears of importance to understand one of the most classical forms of Markov processes: the Random Walk. In this section we will outline some key differences between the discrete diffusion and its continuous counterpart [22], as these differences will also appear in a less controllable fashion in the bosonic problem when comparing simulations to continuous distributions. In this section we assume all quantities to be unitless.

4.1 Discrete random walk

A 1D random walk for a single particle on a grid is generally described by a master equation:

$$\rho_n(t+\tau) = P_+\rho_{n+1}(t) + P_-\rho_{n-1}(t) \tag{4.1}$$

where $\rho_n(t)$ is the probability for the particle to be on site n at a time t, and τ the time between two jumps. This equation describes the particle's stochastic motion, as it hops left or right (with probabilities P_- and P_+ respectively) after every duration τ.
The particle is launched at $t = 0$ on a given site, which we take for simplicity as site 0. We seek the probability that this particle ends up on site n after N jumps at times $t = N\tau$. Since the system only evolves at discrete times, we know that the particle will do a number of left/right jumps n_-/n_+, which verify $N = n_+ + n_-$ and $n_+ - n_- = 2n_+ - N = n$. The sought after probability is a binomial distribution: $\rho_n(t = N\tau) = P_+^{n_+}P_-^{n_-}\binom{N}{n_+}$, the probability of drawing n_+ right hops in N total draws. Assuming $P_+ = P_- = 1/2$,

$$\rho_n(t) = \left(\frac{1}{2}\right)^N N!\left[\left(\frac{N+n}{2}\right)!\left(\frac{N-n}{2}\right)!\right]^{-1}\Bigg|_{N=\frac{t}{\tau}} \tag{4.2}$$

This distribution can be used to compute the average distance reached $\langle n\rangle = 0$ and the distributions spread:

$$\langle n^2\rangle = \sum_n n^2\rho_n(t) = \sqrt{N} = \sqrt{t/\tau} \tag{4.3}$$

4.2 Continuous limit: Wiener process

To take a continuum limit of eq. (4.1), we start by recasting the equation in the following shape, introducing the step size Δ, which corresponds to the grid width (assuming $P_+ = P_- = 1/2$):

$$\frac{\rho_n(t+\tau) - \rho_n(t)}{\tau} = \frac{\Delta^2}{2\tau}\left[\frac{\rho_{n+1}(t) - 2\rho_n(t) + \rho_{n-1}(t)}{\Delta^2}\right]$$

We now switch notation $\rho(x,t) = \rho_n(t)$, where x is a continuous coordinate, on which sites are identified as $x_n = n\Delta$ (n integer). We then take the continuum limit $\Delta \to 0$, $\tau \to 0$, which yields a diffusion equation, also known as the master equation of the Wiener process:

$$\dot{\rho} = D\frac{\partial^2 \rho}{\partial x^2} \tag{4.4}$$

with diffusion constant $D = \frac{\Delta^2}{2\tau}$. Eq.4.4 is solved by

$$\rho(x,t) = \frac{1}{\sqrt{4\pi D t}} e^{-x^2/4Dt} \tag{4.5}$$

with the initial condition $\rho(x,0) = \delta(x)$. This implies that the average spread of the probability distribution follows:

$$\sqrt{\langle x^2 \rangle} = \left[\int_{-\infty}^{+\infty} x^2 \rho(x,t) dx\right]^{\frac{1}{2}} = \sqrt{2Dt} \tag{4.6}$$

It should be noted that the large N limit (large number of steps or equiv. large times) of the binomial distribution (4.2) is a Gaussian distribution. The discrete and the continuous distributions can be matched: $\rho(x, t \to \infty) = \frac{1}{2\Delta}\rho_n(t \to \infty)$, fixing $\tau = (2D)^{-1}$. Both discrete and continuous probability densities are plotted in fig.4.1 for a $D = 1/2$ and $\Delta = 1$ diffusion. As expected, the two descriptions coincide at longer times $t > 10$, but they are very different for $t < 1$, due to the very large delta peak in the continuum description.
This result points out that care has to be applied when comparing peaked distributions obtained from continuum descriptions to discrete simulations obtained by Monte-Carlo.

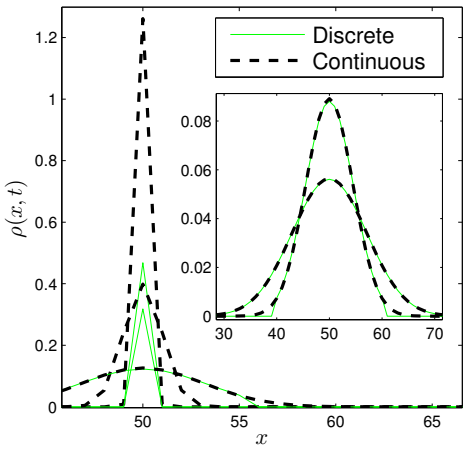

Figure 4.1: $\rho(x,t)$ (black dashed line) and $\frac{1}{2\Delta}\rho_n(t)$ (green continuous line) distributions, plotted at times $t = 0.1$,1,10, and $t = 20$, 50 in the inset, for a random walk with $D = 1/2$, $\Delta = 1$. Initial conditions: $\rho_n(0) = \delta_{n,50}$ and $\rho(x,0) = \delta(x-50)$. At short times, the continuous delta totally overestimates the discrete probability, but both discrete and continuous models converge at larger times. For $t \leq 10$, the center sections of the distributions coincide, but the tails of the distributions still show slight differences up to $t = 20$, which even out at later times.

CHAPTER 5

Anomalous diffusion, analytics

In sect. 3.2 we have understood that the many-body quantum problem (3.1) could be mapped onto a classical master equation with non-uniform diffusion factors, eq. (3.11). In this section, we address some analytical mean-field predictions that have been made for the system and sketch how they have been derived. A more detailed comparison to the numerical results of the full system are to be found in sect. 8. The contents of sections 5.1, 5.2 and 5.2.2 has been introduced for two sites in [4] and [5], and for L sites in [6].

5.1 Decoupling the equations

Starting from eq. (3.11), we introduce the mean-field (MF) ansatz:

$$\rho = \otimes_m \rho_m^m \left|m\right\rangle \left\langle m\right| \tag{5.1}$$

where ρ_m^m is a 1-site density matrix element. This assumption decouples the density matrix elements ($\rho_{\cdot,\cdot}^{\cdot,l,m,n,\cdot,\cdot} = ...\rho_l^l \rho_m^m \rho_n^n ...$) to single site contributions. What the ansatz effectively does is drop all correlations in the anomalous walk, and assume that a given site density matrix element ρ_m^m 'sees' an average distribution resulting from the average of all the other sites, hence the mean-field denomination. In general, it is rare that a MF approximation correctly accounts for a system's dynamics in 1 dimension, but sometimes it will at least correctly predict the critical exponents. As we will see, this mean-field system will point out some important features of the full system, and give accurate results for very short times (before neighbor correlations grow too much).
Plugging ansatz (5.1) into eq. (3.11), and switching notation $\rho_m^m(t) = \rho_m(t)$ leads to

$$\begin{aligned}
\partial_t \rho_m = -\frac{2zJ^2\Gamma}{\hbar} \quad & \left[\sum_l \frac{(l+1)m}{(l-m+1)^2U^2+\Gamma^2} \rho_l \rho_m \right. \\
+ \quad & \sum_l \frac{(m+1)l}{(m-l+1)^2U^2+\Gamma^2} \rho_l \rho_m \\
- \quad & \sum_l \frac{(m+1)l}{(m-l+1)^2U^2+\Gamma^2} \rho_{l-1} \rho_{m+1} \\
- \quad & \left. \sum_l \frac{(l+1)m}{(l-m+1)^2U^2+\Gamma^2} \rho_{l+1} \rho_{m-1} \right]
\end{aligned}$$

Where z is the number of nearest neighbors in the system geometry (2 in our 1D case). Here we introduce the rescaling of t (defined from continuum limit, see sect. 5.2):

$$\tau = t \cdot \frac{2z\Gamma J^2}{\hbar f^2 U^2} \tag{5.2}$$

The mean-field master equation thus becomes:

$$\begin{aligned}\partial_\tau \rho_m = -f^2 \quad & \Bigg[\sum_l \frac{(l+1)m}{(l-m+1)^2 + (\Gamma/U)^2} \rho_l \rho_m \\ + & \sum_l \frac{(m+1)l}{(m-l+1)^2 + (\Gamma/U)^2} \rho_l \rho_m \\ - & \sum_l \frac{(m+1)l}{(m-l+1)^2 + (\Gamma/U)^2} \rho_{l-1} \rho_{m+1} \\ - & \sum_l \frac{(l+1)m}{(l-m+1)^2 + (\Gamma/U)^2} \rho_{l+1} \rho_{m-1} \Bigg]\end{aligned} \tag{5.3}$$

The numerical solution to this equation is straightforward to obtain. This a 1st order differential equation of dimension N (particle number), whose solution can be obtained for example with a Runge-Kutta algorithm [23]: The initial $\rho(t = t_0)$ is first set, along with a small timestep Δt. An arbitrary $\rho(t)$ can then be reached by steps of Δt, calculating $\rho(t_0 + \Delta t), \rho(t_0 + 2\Delta t), ..., \rho(t)$ by numerical approximation of the derivative in eq. (5.3). In these simulations, error is well controlled, as it only depends on Δt, and on the order of the method. For example a second order Runge-Kutta algorithm will have a $\mathcal{O}((\Delta t)^3)$ error per time step. In the following sections, all curves refered to as 'MF decoupled' or 'MF' come from such a computation [24].

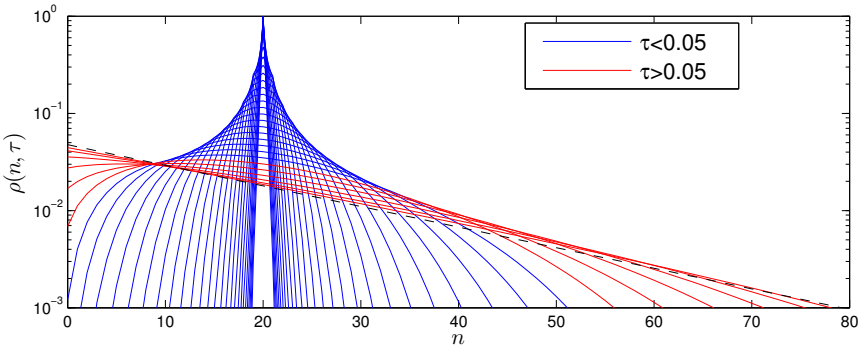

Figure 5.1: Mean field numerically obtained [24] distribution of the density matrix elements $\rho_n(t) = \rho(n, \tau)$ over rescaled times ranging from 10^{-8} to 2. The fast broadening of the distribution is associated with a gradual increase of asymmetry. This behavior gets more pronounced once the boundary $x = 0$ is reached. Note that the distribution converges towards the infinite system steady state ρ_n^∞ (black dashed line). $f = 20$, $U = 5$.

In the next few sections, we will first study the very short term evolution, before taking a continuum limit of (5.3) to study the dynamics on a longer timescale.

5.1.1 Short term evolution

To understand the very first regime of the dynamics, we may use eq. (5.3) as basis. At $\tau = 0$ we suppose that the system is prepared in a Mott insulating state of filling f, i.e. $\rho_m(0) = \delta_{mf}$. Substituting this into eq. 5.3

directly yields the relevant density matrix elements, from which the initial behavior of the fluctuations can be deduced:

$$\rho_f(\tau) = \frac{1}{f^2} - 2f\frac{f+1}{1+(\Gamma/U)^2}\tau \tag{5.4}$$

$$\rho_{f\pm1}(\tau) = f\frac{f+1}{1+(\Gamma/U)^2}\tau \tag{5.5}$$

$$\frac{\kappa(\tau)}{f^2} = \frac{\sum_n n^2\rho_n - f^2}{f^2} = f\frac{f+1}{1+(\Gamma/U)^2}\tau \tag{5.6}$$

As we see, this initial behavior is characterized by a linear rise of the fluctuations, rooted in a linear rise of the $\rho_{f\pm1}$ elements. Physical interpretation of this result is discussed in sect. 8.3, but we may already predict that this is related to statistics of the first jump in the system. Clearly this approach breaks down as $\rho_{f\pm2}$ and higher/lower excitations rise. At later times, the dynamics depend on the interplay of a high number of different excitations, which we will treat with a more powerful method, described in the next section.

5.2 Continuum description

Once the master equation has been decoupled to an on-site density matrix description (eq. (5.3)), it is possible to derive a continuum description. The continuum limit is valid for large fillings as we take as continuous variable $x = n/f$. The continuous on-site occupation number distribution will be written as $p(x = n/f) = f\rho_n$, and the decoupled master equation can be written as the following integro-differential equation:

$$\frac{\partial p(x,\tau)}{\partial\tau} = \frac{\partial}{\partial x}\left[D(x,\tau)\frac{\partial p(x,\tau)}{\partial x} + F(x,\tau)p(x,\tau)\right] \tag{5.7}$$

where

$$D(x,\tau) = \int_0^\infty \frac{xy}{(x-y)^2+\varepsilon^2}\,p(y,\tau)\,dy, \tag{5.8a}$$

$$F(x,\tau) = \int_0^\infty \frac{xy}{(x-y)^2+\varepsilon^2}\,\partial_y p(y,\tau)\,dy \tag{5.8b}$$

and $\varepsilon = \Gamma/fU$. This is a non-linear diffusion equation where the diffusion function $D(x,\tau)$ and the force field $F(x,\tau)$ depend on the distribution function $p(x,\tau)$. Notice here that the total probability is still conserved ($\int_0^\infty p(x,\tau)\mathrm{d}x = 1$). Further, it can be shown that the asymptotic solution of (5.7) is $p(x,\infty) = e^{-x}$, corresponding to the large f limit of the discrete one-site reduced density matrix: $p(x,\infty) = f\rho_{xf}^\infty = (1+1/f)^{-1-fx} = e^{(-1-fx)ln(1+1/f)} \approx e^{-1/f-x} \approx e^{-x}$.
This continuum description is a good approximation for the discrete behavior at finite ε, for large fillings f, assuming that $p(x,\tau)$ varies smoothly on scales of the order of $1/f$. In our case, we will consider a strongly peaked initial state $p(x,0) = \delta(x-1)$. Strong variations of the distribution will occur at initial times (an artifact of the continuous δ function), but the description is accurate at longer times. This continuum description will allow us to show that an initial anomalous diffusion power law regime will be followed by a slow stretched exponential relaxation towards the steady state.

5.2.1 Sub-diffusive regime

Our system is initially prepared in a peaked distribution at $x = 1$. For such a distribution the force term is negligible, and we can approximate the diffusion equation by $\partial_\tau p(x,\tau) = \partial_x\left[\frac{1}{(x-1)^2+\varepsilon^2}\partial_x p(x,\tau)\right]$. In the $\varepsilon \to 0$ limit (large interaction/filling limit), this equation is analytically solvable, and yields an anomalous diffusion:

$$p(x,\tau) = \frac{1}{4\,\Gamma(5/4)\,\tau^{1/4}}e^{-\frac{(x-1)^4}{16\tau}} \tag{5.9}$$

where $\Gamma(s)$ is the gamma function [31]. Using this result, the local number fluctuations can also be deduced:

$$\kappa/f^2 = \int_0^\infty (x^2-1)p(x,\tau)dx = \frac{\Gamma(3/4)}{\Gamma(5/4)}\sqrt{\tau} \tag{5.10}$$

We see that both the probability distribution $p(1,\tau)$ and the fluctuations κ exhibit a power law regime. The predictions for κ are in good agreement with the MF simulation for $\tau \ll 1$, as shown for a set of parameters in fig. 5.2 and in greater detail in [6]. The spread of the probability density $\sqrt{\langle x^2\rangle} \sim \tau^{1/4}$ is much slower than the one obtained in Brownian motion ($\sqrt{\langle x^2\rangle} \sim \tau^{1/2}$, sect. 4), hence the 'sub-diffusion'. This is primarily due to the non-homogeneous divergent diffusion factor $D(x) \sim 1/(x-1)^2$ for $x \sim 1$. Physically this heating regime corresponds to a fast broadening of the distribution function (see fig. 5.1), gradually creating small particle fluctuations around the average value. As time advances, we expect the non-homogeneous diffusion factor and the force term to lead the system to an asymmetric distribution. This behavior will become remarkable once the distribution comes close to the $x = 0$ boundary (see fig. 5.1, the strongly non-symmetric red curves are in the regime where κ leaves the power law regime).

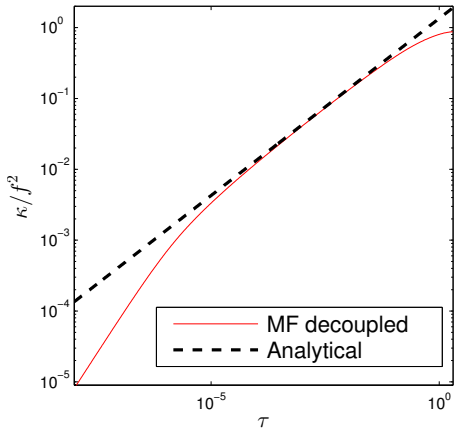

Figure 5.2: Density matrix distribution: MF decoupled numerics (from eq. (5.3), [24]) and the continuum description analytical result (5.10), for $f = 20$, $U = 5$. We observe a good agreement between the two over roughly 4 orders of magnitude.

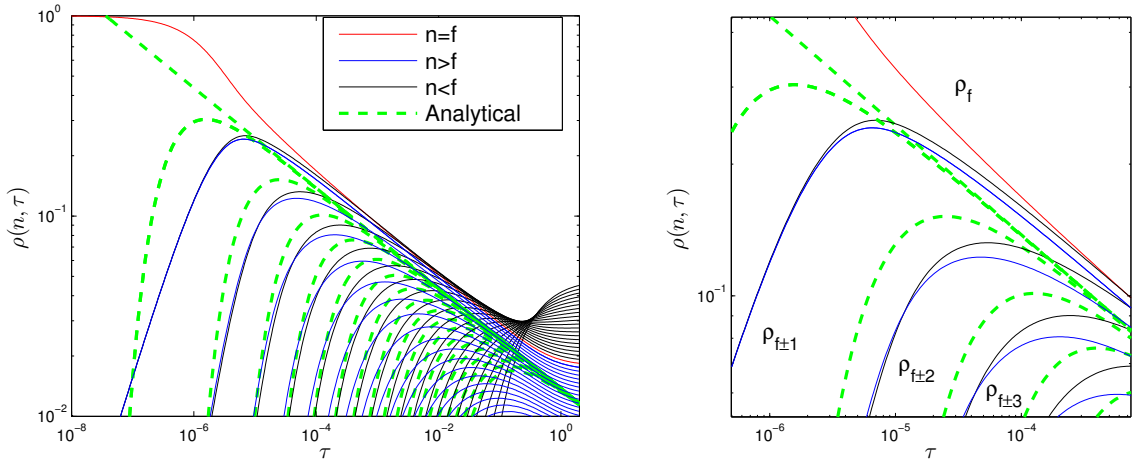

(a) (b) Zoom on (a)

Figure 5.3: The density matrix numerical mean field simulation [24] plotted versus time. The balanced ($\rho(f,\tau)$, in red), as well as the unbalanced ($\rho(n,\tau)$, $n \neq f$ in blue/black) are shown along with the analytical result (5.9). Although the calculations predict the correct power law, a discrepancy is observed, due to the fact that the ρ_n distribution isn't symmetric already very early in the simulation. $f = 20$, $U = 5$.

When directly plotting the matrix elements as a function of time (fig. 5.3), we note some deviations to the analytical prediction (5.9). The discrepancies are due to continuous versus discrete effects, as well as asymmetry effects. The numerical solution ρ_f (this configuration probability is plotted in red) exhibits a

clear $\sim 1/\tau^{1/4}$ power law regime, but its pre-factors are not in agreement with the analytical prefactors. The asymmetry effects can be seen in fig. 5.3 (b): the $\rho_{f\pm1}$ are identical up to $2 \cdot 10^{-6}$, were they start splitting up. This clear indication of asymmetry is noted for all ρ_n elements, and inevitably leads to a discrepancy with the calculations. The reason why the κ curve shows such a nice agreement is that the (x^2-1) factor in integral (5.10) picks out only the symmetric contributions of the distribution. Note that this power law regime also appears in a 2-site system (see sect. 7, [5] or [4]).

5.2.2 Long time evolution

Once the system leaves the power law regime, the combined action of the diffusion factor and the force term will drive the system towards the steady state $p(x,\infty) = e^{-x}$. This exponential suppression of large x values yields an important physical observation: Large x realizations (piles with a large occupation) have very slow evolution rates (due to a high energetic cost of transitions to/from high piles), and will thus dominate the long-term dynamics. To understand the interplay of exponential suppression and long-term evolution on the fluctuations, a saddle point argument can be used:

The rare events happen in the tail of the e^{-x} distribution, and are connected by $\propto 1/x$ timescales. Including only these two contributions, $\kappa \sim \int_0^\infty x^2 e^{-x} e^{-\frac{At}{x}}$. The saddle point is determined by $\frac{d}{dx}\left(x + \frac{At}{x}\right)|_{x_0} = 0$ and leads to the main contribution $\kappa \sim e^{-\sqrt{At}}$, which we here identify as a stretched exponential.

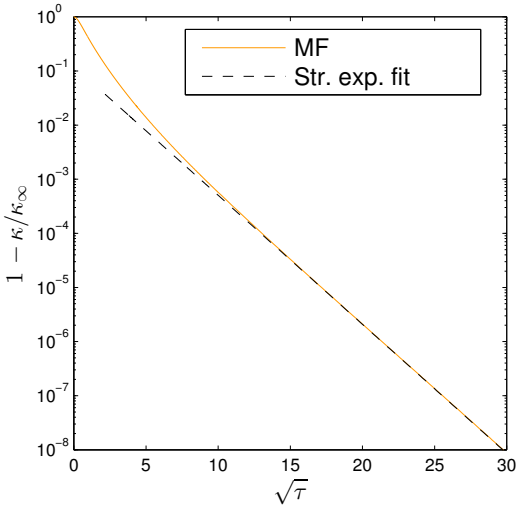

Figure 5.4: The relaxation of the MF fluctuations towards the steady state versus the square root of τ [24]. A stretched exponential behavior is observed, confirming the analytical predictions (5.11).

A more rigorous proof of this finding exists [6], but we will only outline its main steps here: The derivation relies on the fact that the final relaxation is fast for small values of x. Therefore, the evolution at longer times is governed by the population of the tail of the e^{-x} distribution, while very little changes at low x. First, the main contributions at large x are identified in the diffusion and force term: $D(x,\tau) \approx -F(x,\tau) \approx \frac{1}{x}$. The relaxation towards the final state is then described by the ansatz $p(x,\tau) = p(x,\infty)g(x,\tau)$, where $g(x,\tau)$ can be identified as an error function [31]: $g(x,\tau) = \frac{1}{2}\left\{1 - \mathrm{erf}\left[\frac{\sqrt{3}}{2}\,\frac{x-\sqrt{2\tau}}{(2\tau)^{1/4}}\right]\right\}$. From there the fluctuations can be obtained:

$$\kappa_\infty - \kappa(\tau) \propto h(\tau)\, e^{-\frac{3}{2}\sqrt{\frac{\tau}{2}}} \tag{5.11}$$

where h depends algebraically on τ. We have thus shown that at long times the MF system's relaxation to the steady state slows down. We showed that the decay was of stretched exponential form, emerging due to the interplay of kinetic and interaction energy in the heating process. This stretched exponential behavior is shown in fig.(5.4) for $f = 1$, and it can be shown that this behavior arises for all fillings, later in time for higher fillings.

It is clear that, due to a rise of correlations, the MF picture may not accurately describe the dynamics of the full system (3.11), and it will therefore be among the main concerns in the Monte Carlo Simulations to understand which features of the MF approach survive.

CHAPTER 6

The Monte-Carlo algorithm

The Monte-Carlo (MC) algorithm was first coined in the late 1940's to 1950's with the arrival of the first computers, and was thought of as a more practical method over "abstract thinking" to solve a problem [27]. A typical example of this is the direct sampling method to solve integrals, where the idea is to randomly distribute points within a boundary, and determining the area of an enclosed region (for example a circle within a square), by counting the ratio of hits in each part of the surface (see fig.6.1, or [25]).

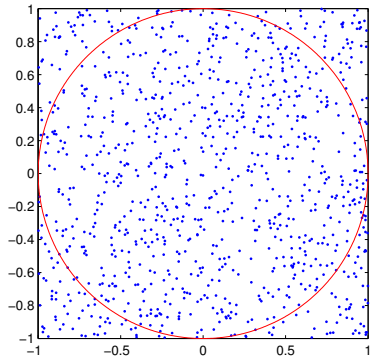

Figure 6.1: 1000 points are drawn in the $(-1,1) \otimes (-1,1)$ domain. The ratio of the number of hits in the circle and the total draws multiplied by the area of the square gives us an estimation of $\pi \sim 4\frac{N_{\text{hits}}}{N_{\text{total}}} = 3.152$

In general, Monte-Carlo methods are a class of computational algorithms that rely on repeated random number sampling to compute results. Even though the mentioned integration method is not efficient in a 2D case in comparison to say a trapeze method, its value is quickly understood in computing integrals in higher dimensions. The usual field of application of Monte-Carlo algorithms is problems where deterministic algorithms become infeasible due to a high number of system variables. Nowadays these range from statistical physics, quantum physics, mathematical, financial, biological, and chemical systems to name just a few.

In our case we will not be interested in solving integrals, but rather want to sample the evolution of a Markov chain , i.e. a random process characterized by transitions between a finite number of states. We have justified in sect. 3 that our bosonic system can be described by a master equation:

$$\dot{\rho}_{\mathbf{n}} = \sum_{\mathbf{m}} [W_{\mathbf{nm}}\rho_{\mathbf{m}} - W_{\mathbf{mn}}\rho_{\mathbf{n}}] \tag{6.1}$$

where the $\mathbf{n}$ index references a configuration of the system ($...l, m, n, ...$ in our bosonic system), $\rho_{\mathbf{n}}$ is the density matrix element corresponding to that configuration (the probability to realize the state) and $W_{\mathbf{mn}}$ is the transition rate from state $\mathbf{n}$ to $\mathbf{m}$.

Monte-Carlo sampling of such a master equation essentially consists in executing trial runs of the markovian evolution, and then to extract average observables from the obtained statistics: say $\mathbf{n_0}$ is the initial

configuration of the system, one then needs to draw a new configuration $\mathbf{m}$, taking into consideration the probability of transition to each state. Once a new configuration is drawn the system is evolved and the operation repeated until the desired time is reached. This yields one trajectory of the system, and the simulation then needs to be repeated several times (typically ~ 100 to several millions, depending on the system) to understand the average behavior of the system.
In fig. 6.2a we plot 40 different trajectories of a random walk starting on site 50. To understand the average behavior of a walker, we can for example plot the distribution of walkers over the sites, at different times. This is done in fig. 6.2b where we compare the discrete Monte-Carlo distribution to the analytically derived continuum limit (4.5), for times $t = 10$ and $t = 200$. For these time values we expect a good agreement (recall fig. 4.1), and we note that at least 1000 runs are needed to correctly sample the distribution at large times.

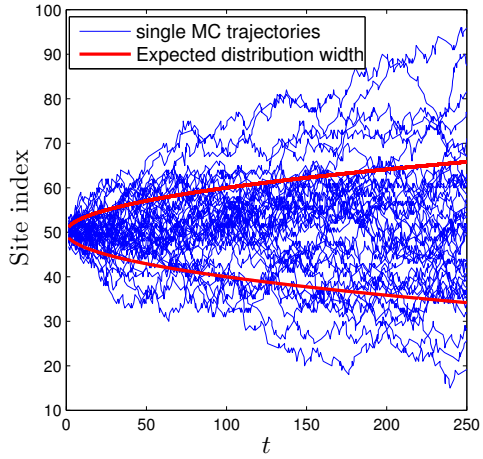

(a) 40 different trajectories plotted versus time, as well as the analytical mean width of the distribution

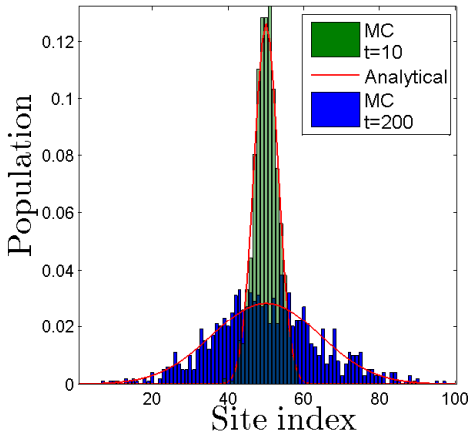

(b) Population distribution at two times, compared to the analytical distribution (4.5), for 1000 independent single particle runs.

Figure 6.2: Monte-Carlo simulation of a random walk with $D = 1$. A large number of runs are representative of the analytical distribution described in sect. 4

It should be noted here that using the same algorithm one can also describe the evolution of an initial distribution, by doing an extra sampling over the initial configuration. To be precise, one first needs to generate a set of initial configurations $\mathcal{N} = \{\mathbf{n}, \mathbf{n'}, ...\}$ that account for the initial statistical superposition, i.e. $\rho(t = t_0) = \sum_{\mathbf{n}\in\mathcal{N}} \rho_{\mathbf{n}} |\mathbf{n}\rangle \langle\mathbf{n}|$. Using this, the system's evolution is then approximated by Monte-Carlo sampling each single initial state of $\mathcal{N}$ independently, and then observing the average behavior.
When designing an algorithm, the key points are drawing the next state efficiently and correctly tracking time. A few methods will be presented in sections 6.1 and 6.2.

6.1 Rejection-prone algorithm

There are several ways to solve the problem with a so-called rejection algorithm. An initial configuration $\mathbf{n}$ is given, and the transition rates to all other possible states $\mathbf{n}'$ are known: $W_{\mathbf{n}'\mathbf{n}}$. One should then start by fixing a small timestep Δt, which gives us the transition probabilities $W_{\mathbf{n}'\mathbf{n}}\Delta t$ (for this to be true one should theoretically have $\Delta t \to 0$).
A first solution would be to draw a random site, draw a random hopping direction, and accept this hop with probability $W_{\mathbf{n}'\mathbf{n}}\Delta t$. Clearly this is inefficient, since every draw has a high rejection rate.
Another, more efficient solution would be to make a 2D random draw in a domain $(0, 1) \otimes (0, W_{\max})$ where

different zones would have initially been delimited, proportional to the different transition rates: If there are K possible transitions, we could conceive K boxes tiled next to each other on a $(0,1)$ axis, the height of the domain given by the largest rate $W_{\max}$ (see fig.6.3 (a) or [25]). The area in which the draw falls would correspond to the next state, and if the draw falls outside a box, the draw needs to be re-done (it is rejected). Both mentioned methods have a major flaw though, and that is that Δt may need to be chosen very small to conserve probability, and a high rejection rate is induced, if the rates vary too much. Indeed, for example if 3 transitions are possible, of rates $W_{\mathbf{1n},\mathbf{2n},\mathbf{3n}} = 1, 1, 100$, it appears that the rejection area in our second construction would be $2/3 * 0,9 = 60\%$ of the total area, while the time step Δt can't be chosen larger than $1/\sum_{\mathbf{i}} W_{\mathbf{i}} \sim 0.01$.
This algorithm can be very efficient in the case where the rates are all of the same order of magnitude. Even if rejection occurs, the small computational cost of the algorithm (the heaviest operation is to determine the maximum rate) can outweigh rejection free algorithms (a rejection method is for example the Metropolis algorithm [25]). In our system however, a plot of the transition rates as a function of the neighboring population reveals that these vary over several orders of magnitude (see fig.(6.3(b))). Such a rejection method is therefore not viable.

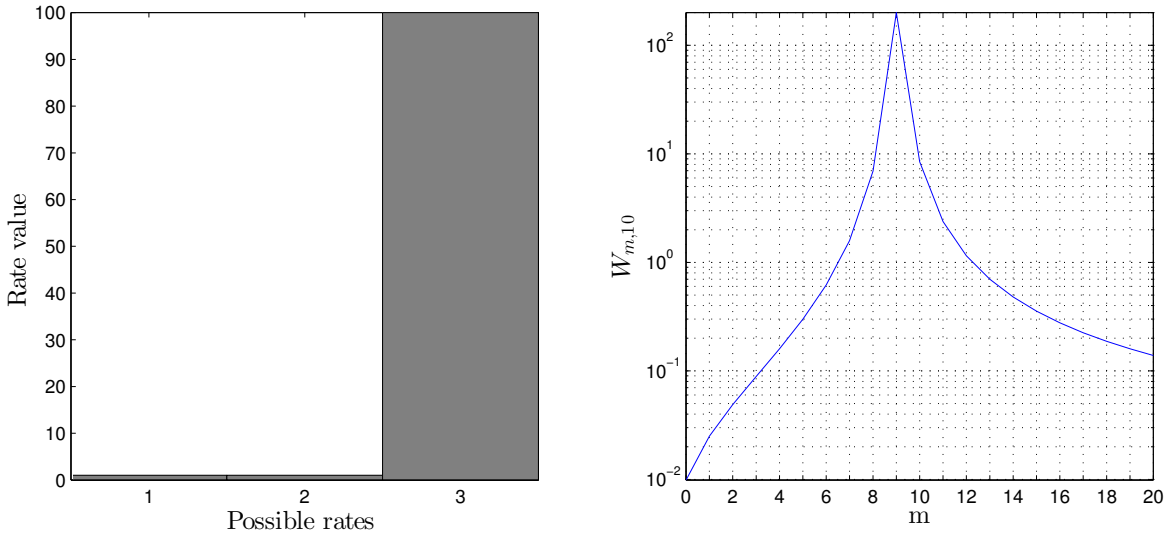

(a) (b)

Figure 6.3: (a): A schematic of the construction mentioned in the text for a rejection algorithm. The rates are tiled next to each other, and a draw is done in the domain $(0,1) \otimes (0, W_{\max})$. The possible rates are $W_{\mathbf{1n},\mathbf{2n},\mathbf{3n}} = 1, 1, 100$, $W_{\max} = 100$ in this case. (b): In the bosonic system under study, this is the hopping rate from a site with population 10 to a neighboring site with population m. We first notice that these rates cover 4 orders of magnitude, rendering rejection methods totally unfeasible. The exact shape of the curve and its consequences on the system will be discussed in the following chapters.

6.2 Rejection-free algorithm

To sample the master equation more efficiently, one needs to avoid rejection, and this can be done by using a Kinetic Monte-Carlo algorithm (see[28], [29] or [30]), doing so-called tower sampling [25]: Instead of regularly testing the system, one first determines the waiting time in the given state (one draws the waiting time from its distribution), and one only draws for a movement once the waiting time is over.

Drawing the holding time: Given a state **n** a time $t = 0$, the probability the system hasn't escaped yet at time t is related to the cumulated exit rate from state **n**: $p_{survival} = e^{-tW}$, where $W = \sum_{\mathbf{n}'} W_{\mathbf{n}'\mathbf{n}}$. We are interested in the probability distribution of the time of first escape $q(\tau)$. Integrating $q(\tau)$ up to a certain time t gives us the probability that the system has already left the state by time t: $\int_0^t d\tau q(\tau) = 1 - p_{survival}$. Therefore, $q(\tau) = We^{-\tau W}$.
In the algorithm we draw a time step which follows this distribution. To do so, we first invert the relation for $r = q(\tau)$:

$$\tau = -(1/W)ln(r) \tag{6.2}$$

To do the draw, one simply draws a random number with a uniform distribution $r \in]0, 1[$ and replaces it in eq. (6.2) to obtain the holding time.

General procedure: (See also alg.1) The algorithm input is the system's initial configuration. All possible transition rates are first listed in a vector: $W_m = W_{\mathbf{mn}}$ and the cumulated rates $R_i = \sum_{j \leq i} W_j$ are then computed. Now knowing the total exit rate $W = \sum_i W_i$ (the last element of R_i) one can draw the time step from distribution $q(\tau)$, as mentioned in the last paragraph. One then proceeds with the tower sampling: a random number v is drawn in $]0, W]$, and the corresponding rate (If $R_{m-1} < v \leq R_m \Rightarrow$ transition W_m to be executed) is determined through a binary search. One then executes the transition and updates the system: configuration **n** changed to **m**, $t = t + \tau$. Finally, the concerned rates W_i are re-computed as well as the cumulated rates, which completes the loop.
This algorithm is much more efficient than rejection algorithms when the rates cover several orders of magnitude, and it can be shown that the resulting timescales and the dynamics are strictly equivalent [26].

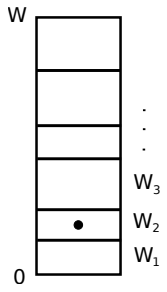

Figure 6.4: An illustration of rejection-free tower sampling. The different outcomes of the transition (W_1, W_2, ...) are virtually 'stacked' on an axis ranging from 0 to $W = \sum_{\mathbf{i}} W_{\mathbf{i}}$, where a transition is finally drawn.

Algorithm 1 Tower sampling, detailed

Input: initial configuration **n**
1. List all $W_m = W_{\mathbf{mn}}$
2. Compute cumulated rates $R_i = \sum_{j \leq i} W_j$

for all MC steps **do**
3. Draw timestep τ from distribution $q(\tau) = We^{-\tau W}$, where $W = \sum_i W_i$
4. Draw a random $v \in]0, W]$
5. Find corresponding jump j: $R_{m-1} < v \leq R_m \Rightarrow$ jump W_m
6. Update system $\mathbf{n} \to \mathbf{m}$, $t = t + \tau$.
   1. Update $W_{\mathbf{i}}$'s
   2. Re-compute cumulated rates $R_i = \sum_{j \leq i} W_j$

end for

Implementing the rates: For the system we consider, the rates depend on the system parameters and the population of the starting and target sites (eq. (3.13)). These need to be separated in left jumps and right jumps. Given a configuration $(n(1), n(2), n(3), .., n(L))$ of the chain (the number of particles on each site), the list of all rates can be written as $\vec{W} = (W_{\underrightarrow{1}}, W_{\underrightarrow{2}}, ..., W_{\underrightarrow{L}}, W_{\underleftarrow{1}}, W_{\underleftarrow{2}}, ..., W_{\underleftarrow{L}})$, where $W_{\underrightarrow{n}}$ is for example a left hop from site n. Periodic boundary conditions are chosen, i.e. $W_{\underrightarrow{L}}$ is a hop from site L to site 1 (to obtain fixed boundary conditions, one simply choses $W_{\underleftarrow{1}} = W_{\underrightarrow{L}} = 0$). The cumulated rates are then

computed from this vector $R_i = \sum_{j \leq i} W_j$, and once an entry is drawn in this vector ($R_{m-1} < v \leq R_m$) it is straightforward to decide on which site the jump should happen and in which direction:

if $m \leq L$ **then**
  Jump right, on site m
else
  Jump left, on site $m - L$
end if

To reduce the system to a normal random walk, a first solution is to sample only 1 particle, with $\Gamma = U = J = 1$, which fixes all rates to 2 (becomes a random walk with diffusion factor $D = 2$). Another solution is to set $W_{\underset{\rightarrow}{i}} = W_{\underset{\leftarrow}{i}} = n(i)$, which yields a $D = 1$ diffusion. In the first case we get a one particle random walk which we sample a number of times to obtain statistics, but in the other we obtain a random walk of several non-interacting particles, where the distribution is directly obtained. Naturally, both are equivalent in average.

Binary search The binary search can be done in roughly $log_2(2L)$ steps (see Alg.2): one inputs an array C of increasing values and a value to search for. At first sight, we are interested in the index j such that $C_{j-1} < value \leq C_j$. One finds the middle of the array and determines whether the value searched for is left or right, and then repeats the procedure until the desired index is reached. Particular care needs to be applied to deal with identical entries and exact matches. An extra condition needs to be added in the algorithm (Alg.2 line 10) for it to return the correct index. For example in a random walk with $D = 1$, where 2 particles are evolved simultaneously: if $N = 2$, $L = 4$, let's say $\mathbf{n} = 0110$. This implies $\vec{W} = 01100110$, and $C = 01111222$. If $value = 0.1$, the algorithm returns $j = 2$, and if $value = 1.1$, it returns 6. But let's now assume $value = 1$. The algorithm starts by finding the middle of the array (index 4) which returns 1. One could then be tempted to exit the loop, since a value meeting the expectation is found, but index 4 corresponds to an unphysical hop from an empty site 4. An extra condition thus needs to be added (Alg.2 line 10) to ensure the code returns the left-most entry with a non-zero rate: $j = 2$, corresponding to a hop to the left from site 2.

Algorithm 2 Binary search

```
1: Input: cumulated rates (C), random number(value)
2: low = 1, high = length(C) − 1
3: while low ≤ high do
4:     j = (low + high)/2 (round to upper Integer)
5:     if C(j) > value then
6:         high = j − 1
7:     else if C(j) < value then
8:         low = j + 1
9:     else
10:        if C(j) ≠ C(j − 1) then
11:            return
12:        end if
13:        high = j − 1
14:    end if
15: end while
16: j = low
```

Computational costs

In the Alg.1, most steps have a computational cost of order L. For example the listing of all the rates (step 1.) is only done once for the full chain and, since updating the system (6.) consists of modifying just a

couple of quantities (in our case just 2 entries in **n** get modified), step 1 just implies updating a few rates (6 rates corresponding to the 6 possible hops concerning the 2 updated entries in **n**). The binary search is done in roughly $log_2(2L)$ steps, but the main computational cost one could expect from the algorithm 1 is the re-summing of cumulated rates (2.), which is of order $O(2L)$ operations in each code iteration.
On the final code at filling $f = 1$, running up to a rescaled time of around 0.1, here are some profiling results on short $\sim 1sec.$ runs (The missing percentages correspond to the execution of all other lines of the code, which tend to be large for such short runs):

- At lengths $L \sim 10$, the binary search takes around 30% of the computation time, and updating the rates(step 1) roughly 30%.
- At lenghts $L \sim 100$, the binary search can take roughly 40% and updating the rates lowers to roughly 10%.
- At $L = 1000$, the code spends roughly 50% of its running time in the binary search, and while updating the system becomes negligible, the re-summing of the rates becomes noticeable: $5 - 10\%$.

We first notice that, as expected, the part of the code that updates the rates becomes negligible as the system size is increased, due to the fixed number of calculations implied. What is however more interesting, is that the binary search clearly dominates the computational time up to $L = 1000$. In general, while the main loop of the Monte-Carlo is executed about 10^4 times to reach about $\tau = 0.1$, the loop in the binary search is executed $log_2(2L) \sim 10$ times more. Here we understand that the binary search plays a very crucial role in the code efficiency for longer runs, and that a straightforward re-summing of the rates is viable even at very long chain sizes.

More elaborate methods exist (binning, log-tree) to reduce the cost of the re-summing operation, but they are not necessarily suited for our problem. A nice way of optimizing this would be not to re-sum the array, but to add the new rates at the end of the vector. At the next draw, one would then need to take care to re-draw a value if the last one landed on an already 'used' rate. Like this, apart from the binary search, only $O(1)$ operations would be done per loop, but the number of 'dead' rates would increase over time, leading to more and more rejections. We would then need to fix a threshold on the number of dead rates and re-sum the array from time to time. To use this method, a different bookkeeping technique should be used, but it will only payoff for extremely large chains (over 10000), or on a multi-dimensional code.

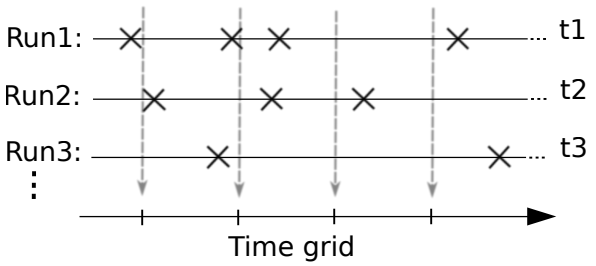

Figure 6.5: An illustration of the measurement process. Each run has its random jump times (cross marks on axes t1,t2,...), but the observables are only written down every time the system passes by an observation point defined by a global time grid (dashed grey arrow).

6.3 Observables, error estimation

To track the evolution of a system, one wishes to study observables, and since these have to be determined from independent runs, a few subtleties have to be addressed, namely tracking the observables at given time points, and error estimation.

Defining an observation time grid

As described in sect. 6.2, individual runs of the simulation will evolve at different times. To average observables between runs, it is important to average them at equal time, and so a global time grid T needs to be

defined beforehand. Every time the system passes by an observation point, the observable is measured. If the system jumps several observation points, the current value of the observable is copied several times. In typical situations, we are interested in the system behavior over long time scales, so the typical observation time will be several orders of magnitude above the typical system evolution time. A pseudo-code realizing the process is shown in alg.3. Additionally, using this technique avoids using unnecessary amounts of memory.

Algorithm 3 Measurement process

Inputs: T: observation time grid (vector), whose last element is T_{max}.
In main MC loop:
(Steps 1,2)
i_{last}: index of last measurement
Draw timestep τ (step 3.)
$t = t + \tau$
while $T(i_{\text{last}}) < T_{\max}$ & $t \geq T(i_{\text{last}} + 1)$ **do**
  Write down current state of observables for time $T(i_{\text{last}} + 1)$
  $i_{\text{last}} = i_{\text{last}} + 1$
end while
(Steps 4,5,6,1,2)

Error estimation

Depending on the observable, error bars can be estimated directly or require a binning technique.

Direct estimation In the bosonic system under study, most of the considered observables don't require knowledge of the distribution of the runs to be evaluated. In this case, observables can be directly averaged over all the runs, and the error can be estimated by assuming a normal distribution: If N is the total number of runs and $\mathcal{O}_i$ is an observable measured in run i, $\langle\mathcal{O}\rangle = \frac{1}{N}\sum_{i=1}^{N}\mathcal{O}_i$, and $\delta(\mathcal{O}) = \frac{1}{N-1}\sqrt{\langle\mathcal{O}^2\rangle - \langle\mathcal{O}\rangle^2}$.

Binning technique For example, in a random walk, an observable of choice is the mean distance to the initial position, corresponding to the spread of the probability distribution function (eq. 4.6). This typically requires the binning technique to estimate errors: M series (bins) of N runs are performed, and the spread of the distribution is measured M times from the statistics of N runs: $\langle x^{(m)}\rangle = \frac{1}{N}\sum_{i=1}^{N} x_i n(x_i)$, and $\sigma^{(m)} = \sqrt{\frac{1}{N}\sum_{i=1}^{N}(x_i - \langle x\rangle)^2 n(x_i)}$. The M observables are then averaged once more over the M bins, and the error bars are extracted assuming M independent quantities: $\sigma = \frac{1}{M}\sum_{i=1}^{M}\sigma^{(m)}$, and $\delta(\sigma) = \sqrt{\frac{1}{M}\sum_{i=1}^{M}(\sigma^{(m)})^2}$. This process is illustrated in fig.6.6, where 5 bins of 50 runs each where computed in a random walk.
Assuming the deviations of the trajectory are normally distributed, it should be noted here that error bars only show the 1σ confidence bounds, i.e. that they only account for roughly 68% of the set. We can however rule out/confirm that the trajectory follows a given law if it comes within the 2σ bounds (since these account for 95% of the set). This is the case in fig.(6.6), where we see that fluctuations can locally push the averaged MC trajectory away from the expected analytical behavior, but these usually stay within 2 error bars.

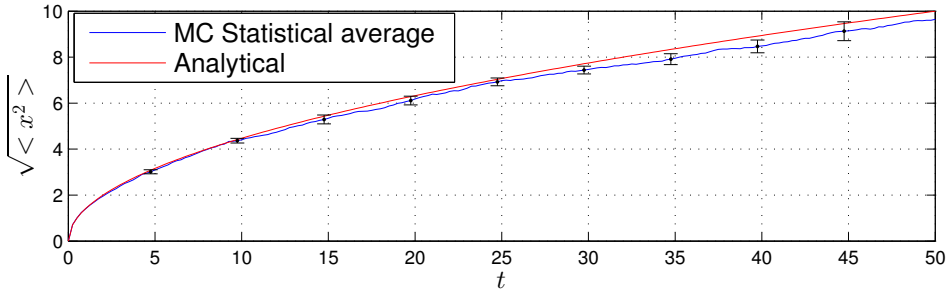

(a) Walker's distance from the origin averaged over 250 runs, as well as the analytical result.

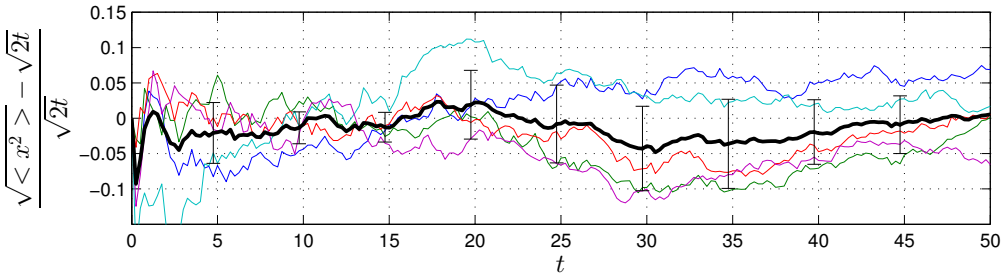

(b) Difference between the MC average and the analytical result. Color lines: the bins used to determine the error bars. Black line: average over all the runs.

Figure 6.6: Random walk with $D = 1$: measurement of the walker's distance as a function of time, 5 bins of 50 trajectories each are used to determine the error bars.

CHAPTER 7

Anomalous diffusion: Monte-Carlo results, two sites

The 2 site dissipative system is well understood (it can be dealt with analytically and numerically, see [5, 4]). Since we wish to focus on the less understood L-site system, the 2 site system will briefly be presented here, as a consistency check of the Monte-Carlo algorithm. In a first section we will show some analytical results, before directly comparing them to MC simulations.

7.1 Outline of analytical results

For the double well configuration, we should first note that a similar approach to the one presented in sections 3 and 5 leads us to an initial power law regime, followed by an exponential decay to the 2-site symmetric steady state. The fundamental steps are in fact identical, to the very crucial difference that the 2-site system does not need the MF decoupling (sect. 5.1), since the adiabatic elimination directly yields an integrable set of equations in the continuum approximation (both approximations are well controlled). More precisely, defining $\hbar\gamma = \Gamma$ (to match the notations in the above mentioned articles), the adiabatic elimination procedure yields the following master equation for the diagonal density matrix elements ($\rho_{n,n}$), valid at times $\gamma t \gg 1$:

$$\partial_\tau \rho_{0,0} = \frac{N}{(N-1)^2}\left(\rho_{1,1} - \rho_{0,0}\right) \tag{7.1a}$$

$$\partial_\tau \rho_{n,n} = \frac{(n+1)(N-n)}{(N-2n-1)^2}\left(\rho_{n+1,n+1} - \rho_{n,n}\right) + \frac{n(N-n+1)}{(N-2n+1)^2}\left(\rho_{n-1,n-1} - \rho_{n,n}\right) \tag{7.1b}$$

$$\partial_\tau \rho_{N,N} = \frac{N}{(N-1)^2}\left(\rho_{N-1,N-1} - \rho_{N,N}\right) \tag{7.1c}$$

for $n \neq \{0, N\}$, N even and $\tau = 2(J^2/U^2)\gamma t$. Here the n index of the matrix elements corresponds to the atom number on one of the sites, the population on the other site being fixed by particle number conservation. Within the large N limit, the discrete master equation is again mapped onto a classical diffusion equation, in which the configuration space is mapped to the coordinate $x = n/N - 1/2 \in [-1/2, 1/2]$, which is a continuous variable in the limit $N \to \infty$. The boundaries of the system become $x = \pm 1/2$ (corresponding to the strongly imbalanced configurations of the double well, $n = 0$ and $n = N$), whereas the center, $x = 0$,

corresponds to the balanced configuration $n = N/2$. The diagonal elements of the density matrix $\hat{\rho}$ are related to the continuum probability density distributions $p(x,\tau)$ via the relation $N\rho_{n,n}(\tau) = p(x,\tau)$. In the continuum, the diffusion equation is:

$$\partial_{\tau_N}\, p(x,\tau_N) = \partial_x \left[D(x)\partial_x p(x,\tau_N)\right] \tag{7.2}$$

where $\tau_N = \tau/N^2$ and $D(x) = \frac{1}{4x^2} - 1$. A solution to this equation is given by:

$$p(x,\tau_N) = \frac{\sqrt{2}}{\Gamma(1/4)} \frac{1}{\tau_N^{1/4}} \exp\left(-x^4/4\tau_N\right) \tag{7.3}$$

from which the local density fluctuations can be computed:

$$\kappa/N^2 = \frac{\sqrt{2}\Gamma(3/4)}{\Gamma(1/4)}\sqrt{\tau} \tag{7.4}$$

Note that this is the same power law as described in sect. 5.2.
After this regime of small fluctuations around the equilibrium configuration, the anomalous diffusion coefficients push the system towards less likely configurations, where the site populations become very imbalanced. Since this pile up can happen on either site, we expect a symmetric steady state (see eq. (3.4)), $\rho_n = \frac{1}{N+1}$. As imbalanced configurations appear, the dynamics slow down, since hopping particles onto the high pile gets more and more suppressed. The imbalanced configurations will thus dominate the long-term evolution, and an exponential relaxation towards the steady state can be predicted due to a finite N effect. In contrast, in the L site system, several of such pileups can arise simultaneously in the chain, giving rise to non-trivial relaxation.

7.2 Comparison to Monte-Carlo simulations

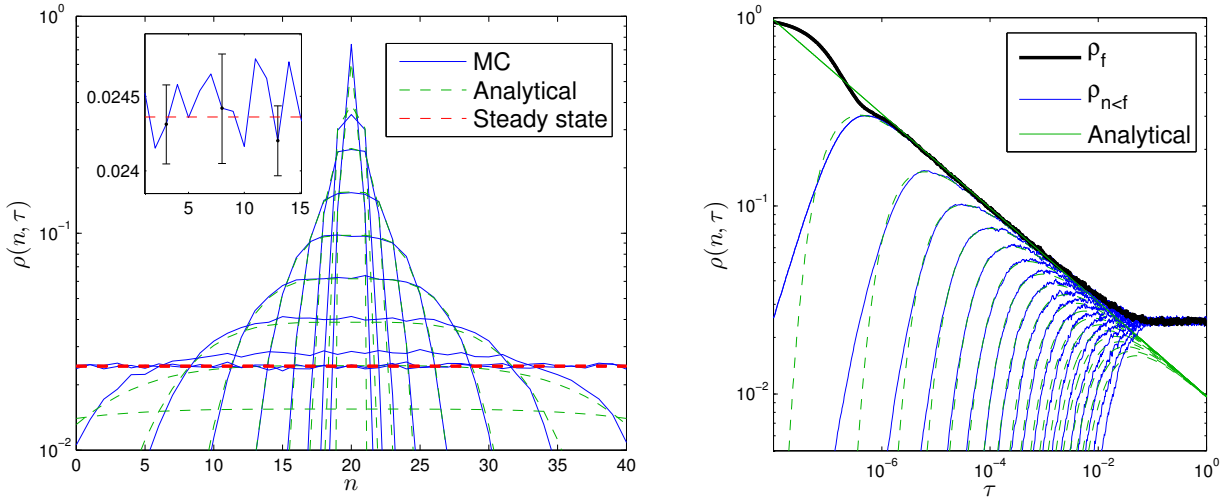

(a) (b)

Figure 7.1: 2 site system: (a) The density matrix element distribution for several (logarithmically spaced) rescaled times raging from 10^{-8} to 1. Inset: zoom on the distribution at $\tau = 1$, compared to the steady state, with some error bars. (b) The density matrix elements as a function of time. The analytical prediction (7.3) is in good agreement with the simulation in a time range from $\tau \approx 10^{-6}$ to $\tau \approx 10^{-3}$, where the system starts relaxing towards the steady state. $N = 40$, $U = 10$, 100000 runs

Fig. 7.1 shows the matrix elements ρ_{nn} behavior as a function of time over 8 orders of magnitude, until the system reaches its steady state, for $N = 40$ and $U = 10$, $\Gamma = 1$. The MC results are plotted versus the analytical result (7.3), and we see excellent agreement from $\tau \approx 10^{-6}$ to $\tau \approx 10^{-3}$. At longer times, due to the increase of totally imbalanced configurations (in fig. 7.1 this corresponds to the moment where the diffusion reaches the $n = 0$ and $n = 40$ boundaries, $x = \pm 1/2$), the system gradually leaves this power law regime to reach its steady state. In this final relaxation we do not expect an agreement to the analytical formula, as it was derived assuming an unbounded diffusion (this is seen for example in fig.7.1(a), where we observe that the analytical distribution keeps spreading beyond the $n = 0$ and $n = 40$ boundaries).
The power law regime predicted analytically in eq. (7.4) is also seen in fig. 7.2, where the local density fluctuations κ/f^2 are shown. The agreement to the analytical result is again very good, although we should note here that this regime is best seen at high fillings $f = N/L$ (see fig. 7.2(a)). Indeed when the filling is decreased, the range of validity of the continuum description also diminishes (for $f = 1$ this regime is not seen, fig. 7.2(a)). In fig. 7.2(b) we also show that the final relaxation follows an exponential behavior.

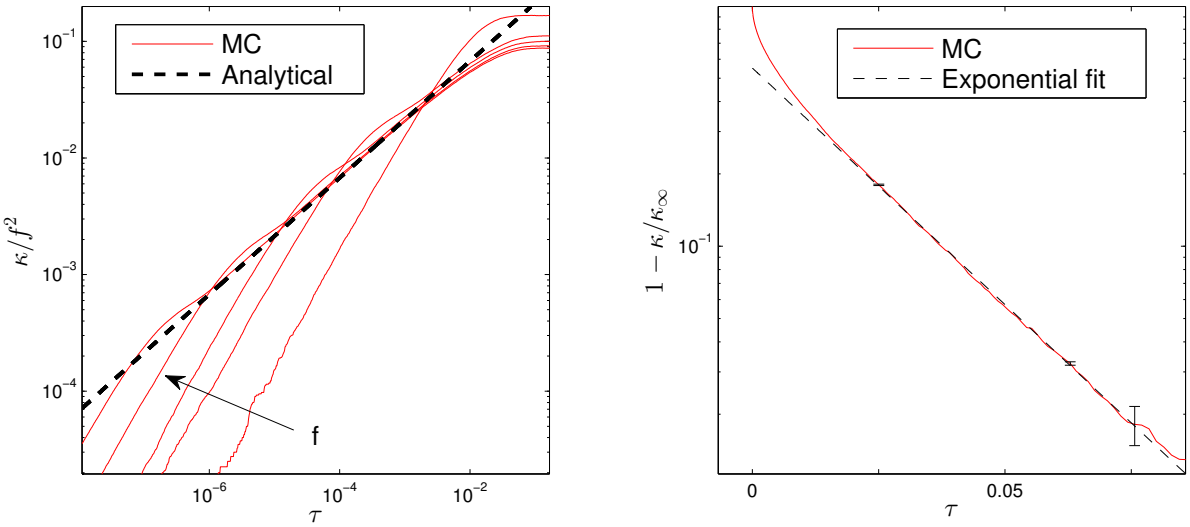

(a) $f = 1, 3, 5, 10, 20$.

(b) $f = 20$.

Figure 7.2: The density fluctuations as a function of time in the 2 site system, where the short (a) and long (b) time behaviors are outlined. In each dynamical regime, a very good agreement is found to the analytical predictions. $U = 10$, $\Gamma = J = 1$, 100000 runs.

CHAPTER 8

Anomalous diffusion: Monte-Carlo results, L sites

This section is the main part of this work. Although the comparison of Monte-Carlo results to mean field predictions will be of prime importance to understand the system dynamics, we will show here that some of the physics is very different from the one obtained within mean field. We will focus on the short, medium and long term dynamics of the system, with a particular importance given to the long-term evolution, where the physics beyond mean-field will be most prominent. We will start with a summary of the system parameters and observables, before presenting an overview of the dynamics.

8.1 L sites: Summary of observables under study, and system parameters

In this section, we will re-define some system parameters, as well as all the observables under study.

System parameters: L: chain length, N: total particle number, $f = N/L$: initial filling, U: particle on-site interaction, Γ: coupling strength to the environment, J: particle hopping parameter, rescaled time: $\tau = t \cdot \frac{4\Gamma J^2}{\hbar f^2 U^2}$.
The hopping rate J is absorbed into the time scale definition, and U will be measured in units of Γ, making L, f and U our only system parameters.

Observables We will consider the following observables ($\langle . \rangle_L$ being an average over the sites and $\langle . \rangle_M$ being an average over M runs):

- The local density on site i: $\langle n_i(t) \rangle_M = \frac{1}{M} \sum_{\text{runs}} n_i(t)$. Due to particle number conservation, $\langle n_i(t) \rangle_{L,M} = f$.
- The local fluctuations (the compressibility) averaged over sites: $\kappa(t)/f^2 = \frac{\langle n_i(t)^2 \rangle_{L,M} - \langle n_i(t) \rangle^2_{L,M}}{f^2} = \frac{\langle n_i(t)^2 \rangle_{L,M} - f^2}{f^2}$.
- The density correlations averaged over sites: $C(d,t)/f^2 = \frac{\langle n_i n_{i+d} \rangle_{L,M}(t) - f^2}{f^2}$.
- The density matrix elements: $\rho(n,\tau) = \rho^n_n(t) = \frac{1}{ML} \sum_{\text{runs,i}} \delta_{n,n_i(t)}$. A binning technique (see sect(6.3)) is needed to extract errors for $\rho(n,\tau)$.

Due to the translational invariance of our problem, observables are first averaged over the sites of the chain (given periodic boundary conditions) before averaging over the runs. With this procedure we gain roughly a factor L in the statistics, and the M averages over runs are totally independent. Error bars can then be extracted with the direct estimation technique mentioned in sect. 6.3, considering the average over sites as basis observable.
A word of caution should, however, be expressed here: if we took the average over the runs first (say to extract observables on a given site j), the observables on each site can then be averaged over the chain, but the error estimation for the final observable then becomes very tedious, since the fluctuations on neighboring sites are correlated.
There is an interesting interpretation of κ in the system under study. In the sampled master equation (3.11) the problem is reduced to motion in the diagonal matrix elements. As a consequence, the average energy is easily computed from (2.6), where the off-diagonal hopping terms vanish:

$$E = \langle H \rangle = \frac{U}{2} \sum_{l=1}^{L} \left(\langle n_l^2 \rangle - \langle n_l \rangle \right) = \frac{UL}{2} \left(\kappa + f^2 - f \right) \tag{8.1}$$

κ is therefore directly related to the total energy of the reduced system. This is a lowest order estimation of the total energy, valid only at large times $t \gg (\Gamma/\hbar)^{-1}$. At short times, there is a non negligible contribution from kinetic energy.

Initial condition In all simulations, we will take as initial condition the Mott insulating state with lattice filling f. This means there are f atoms on each site, which is a peaked distribution in the density matrix elements: $\rho(n,0) = \delta_{nf}$, where δ_{nf} is a Kronecker delta function.

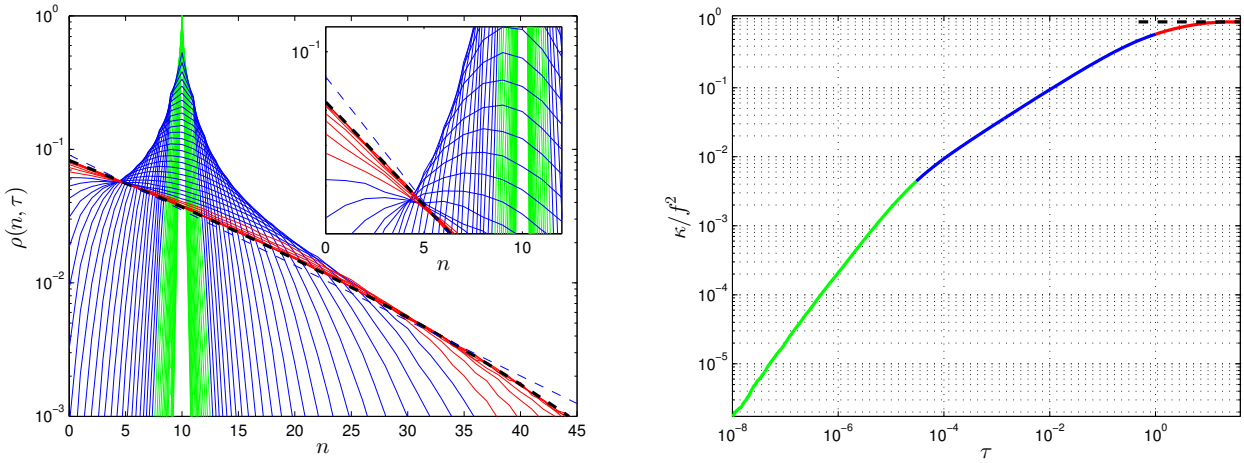

(a) (b)

Figure 8.1: The matrix element's distribution (a) and the local density fluctuations (b) plotted for rescaled times ranging from 10^{-8} to 40. Asymptotic finite system size distribution/fluctuation value: black dashed line. Infinite system distribution: blue dashed line (in(a)). The three colors introduced (green, blue, red), exhibit the 3 different dynamical regimes studied. See text for details. Parameters used: $L = 10$, $f = 10$, $U = 5$.

8.2 Overview

The heating dynamics is characterized by three primary regimes: First, there is a linear broadening of the initially peaked ground state distribution (see fig. 8.1 in green). This regime is associated with the early dynamics, as single atoms start hopping to neighboring sites (see fig. 8.2 in green). These hopping events come from the joint action of dissipation and the tunneling in the Bose-Hubbard Hamiltonian. As time advances, given f large enough, the atom number increasingly fluctuates around the initial filling, resulting in a power law regime (blue regions in fig. 8.1(b)). In this regime, the fluctuations lead to a rapid spread of the density matrix distribution (blue regions in fig. 8.1(a)): configurations far from the atomic Mott state are populated, and repulsive interactions lead to an increase in the system energy (see fig. 8.2(b)). On an even longer timescale, the system relaxes towards its steady state (see red sections in plots, where a finite system relaxation is shown). We will see that this final regime is very sensitive to finite size effects: finite size effects lead to a stretched exponential decay, whereas infinite systems decay in a power law. The final relaxation pattern will be related to a growing time scale within which 2 points are correlated.

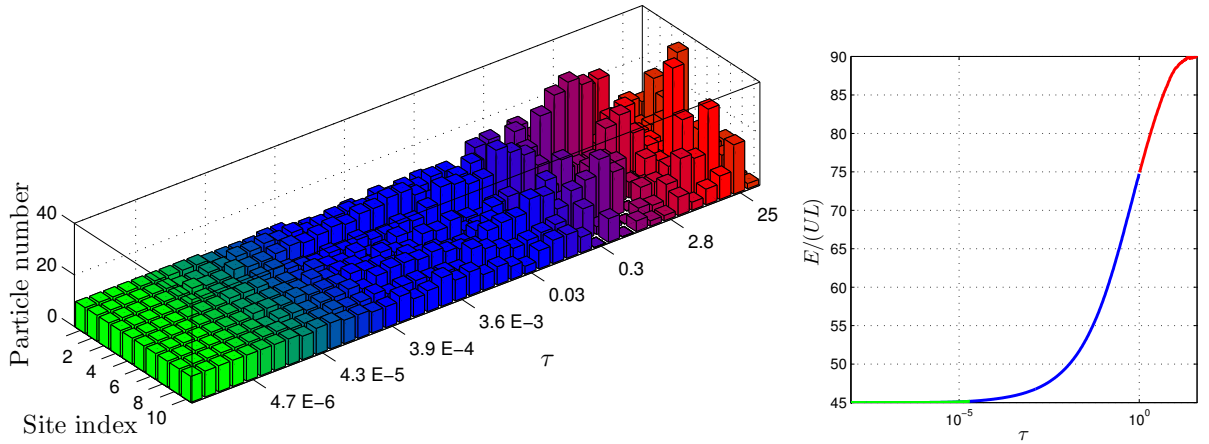

(a) (b)

Figure 8.2: (a) A bar plot of the system state (atom number on each site) versus rescaled time. $L = 10$, $f = 3$, $U = 5$. (b) Plot of the average energy per site, for $L = 10$, $f = 10$, $U = 5$.

8.3 Short-time regime

In section 5.1.1 we have shown that the first instants of the simulation should exhibit a linear rise of the fluctuations and of the first unbalanced density matrix elements. This is confirmed in fig. 8.4(a), where we show that the ρ_f and $\rho_{f\pm1}$ are well described by (5.6) up to $\tau \sim 2 \cdot 10^{-6}$ at $f = 10$. This regime appears at all values of the f (shown for the fluctuation in fig. 8.4 (b)), but the time at which the system leaves this regime (which corresponds to the time at which the elements $\rho_{f\pm2}$ rise) depends on the filling. This is mostly due to the chosen time scale (eq.6.2).
In fig. 8.4 (b) it is also important to point out the behavior of the fluctuations in the MF approximation (shown for $f = 20$). In this very first regime, MF and MC descriptions are equivalent (up to $\tau \sim 2 \cdot 10^{-6}$), but they later split and become parallel. We will explain this difference in the next section.
When the system is prepared in a Mott-insulating state of filling f, the hopping rates between all the sites are equal (for example at $f = 10$, $W_{10,10} \approx 8.5$). However, once the first jump is performed, the population changes to a profile resembling the one in fig.8.3, and several different rates appear: hopping to a neighbor with a slight lesser filling is greatly enhanced, while the hopping to a higher filling is generally suppressed. As a consequence, since very large rates appear, the total rate W as defined in sect. 6.2 will also be large,

leading to an acceleration of the dynamics. Once the first jump is drawn, we see rapid movement of sites of fillings $f \pm 1$, as well as the appearance of new $f+1, f-1$ pairs (see fig.8.5). If however an $f+1$ pile comes close to another $f+1$ site or a $f-1$ site, hopping between them is generally suppressed and another movement is more likely to be drawn. As a consequence, the process is similar to a self-avoiding random walk of the piles in this very first time regime.
If we wait long enough, the system starts building larger piles, as well as deplete sites even further. The system leaves its initial regime and the description based on ρ_f, ρ_{f+1} and ρ_{f-1} breaks down.

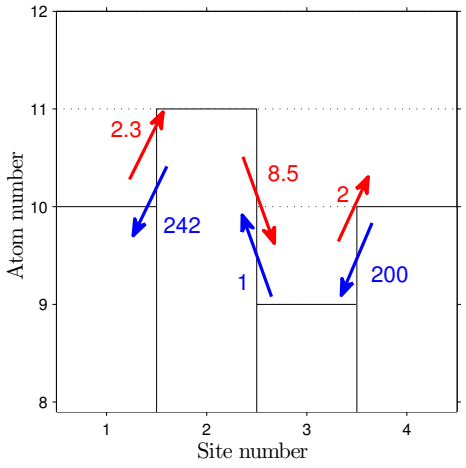

Figure 8.3: (a) The bars represent a given local configuration of the system, while the colored arrows and numbers represent the hopping rates of a particle onto the neighboring site (same as in fig.6.3(b)). We notice that hopping to a neighbor with a slight lesser filling is greatly enhanced, while the hopping to a higher filled site is generally suppressed ($U = 5$).

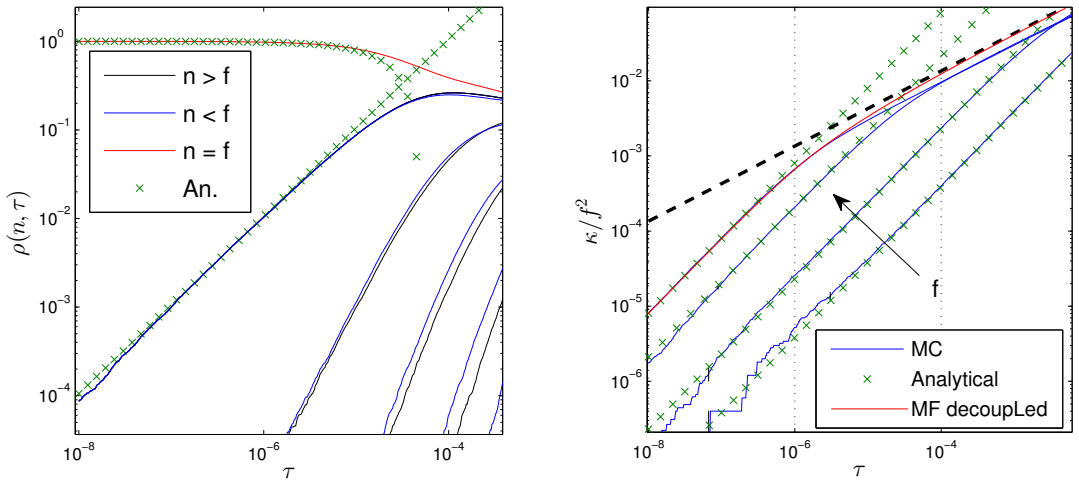

(a) f=10 (b) f=1,3,10,20

Figure 8.4: The density matrix elements (a) and the fluctuations (b) are plotted versus rescaled time, in the early regime of the simulation. An analytical calculation is also show (green crosses), as well as the MF decoupled solution (red curve, [24]). The analytics fit the simulation for various fillings, before the sub-diffusive regime starts ($L = 10$, $U = 5$).

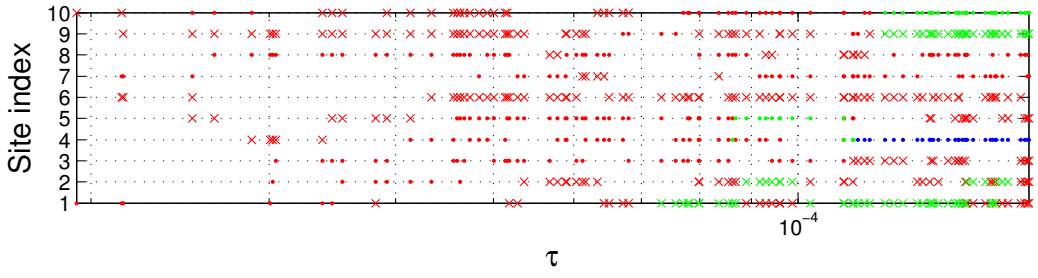

(a)

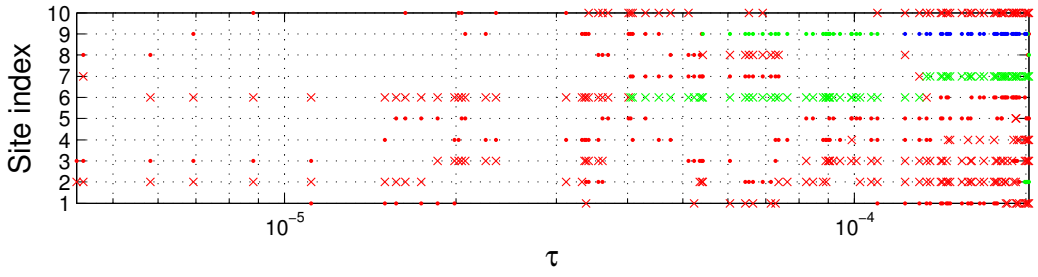

(b)

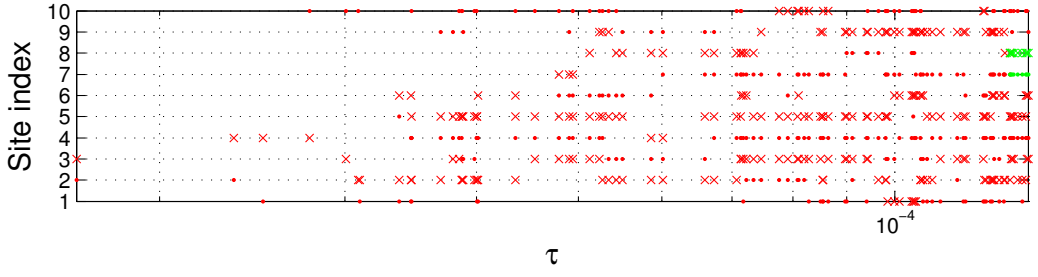

(c)

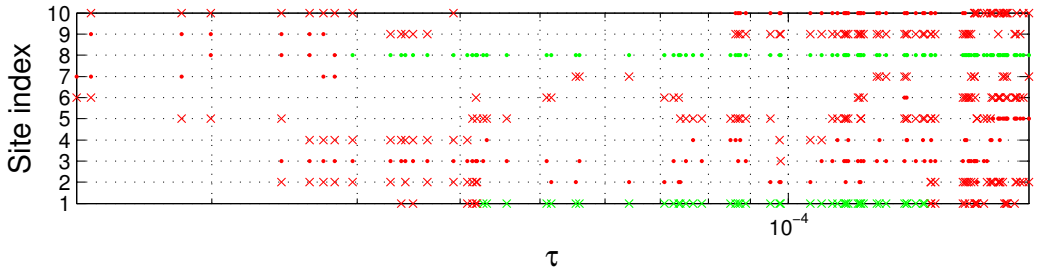

(d)

Figure 8.5: These diagrams show 4 different runs, where the first 100 events in the system are shown (these are not pre-defined time points but the moments where the system effectively changes). These plots should be read from left to right, and the system state is shown every time it changes. '·' stands for a site with filling above f, whereas 'x' is filling below f, while blank spaces are filling f. Red: $n = f \pm 1$, green: $n = f \pm 2$, blue: $n = f \pm 3$. $L = 10$, $f = 10$. Notice the sometimes large blank spaces between the events, this simply happens when the waiting time is drawn in the tail of the distribution (eq.6.2). For example the space just after $\tau = 6 \cdot 10^{-5}$ in run (c) corresponds to a hop from site 5 to site 4, a hop with rate 200 (it is the same jump as from site 4 to 3 in fig.8.3) [32]. In our model the waiting time and the subsequent jump's are not related. $U = 5$.

8.4 Sub-diffusive regime

In the mean-field approach, we expect a power law regime to emerge, associated with the growing of fluctuations (approximately) symmetrically around $n = f$. This results in fast dynamics where piles of various heights are created. Although the real distribution very quickly becomes asymmetric, the approximation to a symmetric distribution allowed us to extract a $\sim \tau^{-1/4}$ power law in the $\rho(f,\tau)$ evolution, and a $\sim \tau^{1/2}$ in the fluctuations.

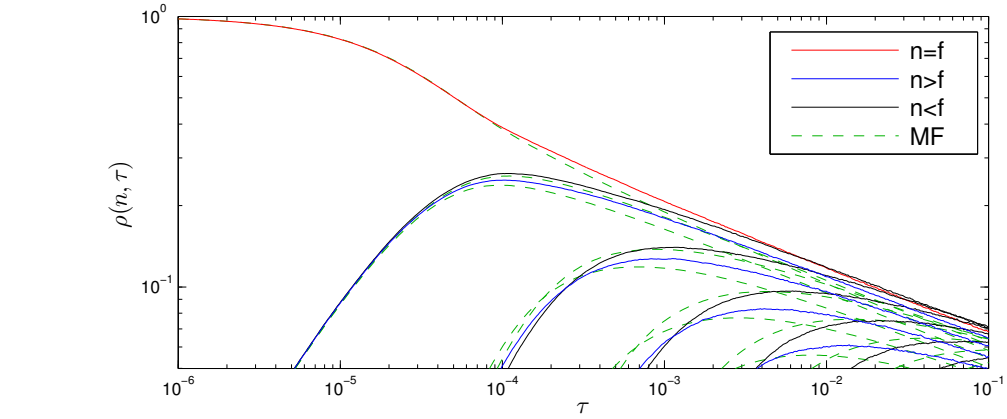

(a)

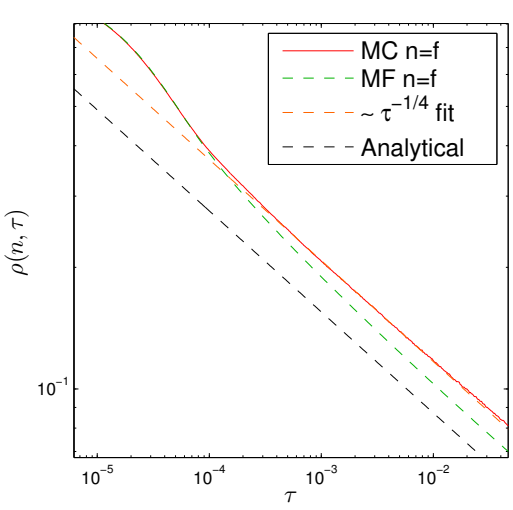

(b)

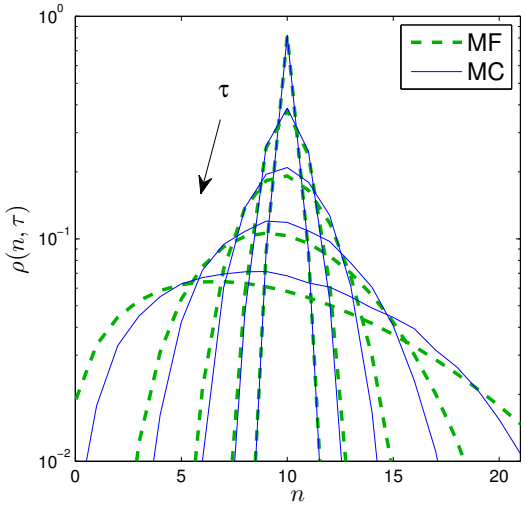

(c)

Figure 8.6: The density matrix elements versus rescaled time, compared to their counterpart in the MF simulation (5.3, [24]). $f = 10$, $U = 5$ ($L = 1000$ and 1100 runs for the MC). In (a) all elements are shown while (b) focuses on the balanced configuration $\rho(f,\tau)$. (b): We note that the MC and MF initially follow the same curve up to $\tau \sim 10^{-4}$, where we note a drift of the MF $n = f$ curve towards the analytical prediction (5.9). The MC follows the same power law as the one predicted in MF, althought the prefactors don't match. (c) The density matrix distribution versus rescaled time, compared to its counterpart in the MF simulation (5.3), at times 10^{-5}, 10^{-4}, 10^{-3}, 10^{-2}, 10^{-1}, $f = 10$. We note that the MF distribution broadens faster than the MC.

In fig. 8.6 (a) and (b) whe plot the $\rho(n,\tau)$ elements as a function of time for a Monte-Carlo simulation with $f = 10$ and $U = 5$. We note that $\rho(f,\tau)$ conforms to a power law behavior for rescaled times 10^{-4} to 10^{-2}, with the same exponent as the one predicted analytically. The MF simulation correctly describes the short-time dynamics, but is not accurate in the sub-diffusivee regime. However, it captures the correct exponent of the power law decay.
In fig. 8.6(c) we plot the $\rho(n,\tau)$ distribution from a Monte-Carlo simulation, and directly compare it to its counterpart in a MF simulation. Both distributions retain a certain asymmetry characteristic of the anomalous rates, but we note that the spread of this distribution is much faster in the MF picture. This is understood by recalling that the MF master equation was obtained by decoupling the L-site density matrix to a 1-site reduced picture. In this representation, the local particle distribution on neighboring sites is independent of the atom number on the considered site. In contrast, the MC simulation, sampled from the complete diagonal master equation, only allows sites to exchange particles if they are neighbors. Effectively this leads to configurations where particle exchange can be hindered due to the anomalous rates. Consider an extreme situation as an example: $\mathbf{n} = (0,5,0,6,0)$. In this configuration, a MF description assumes probabilities $\rho_{n=0} = 3/5$, $\rho_{n=5} = 1/5$ and $\rho_{n=6} = 1/5$. This means that a jump from $n = 5$ to $n = 6$ is possible, which turns out in very rapid evolution due to the small occupancy difference. On the other hand, in the MC simulation, the evolution will be very slow since atom exchange between neighbors is highly suppressed (due to large atom number differences). As a result, in the MC simulation, we expect a slower spread of the matrix element distribution, as we have already noted in fig. 8.6 (a) and (b).

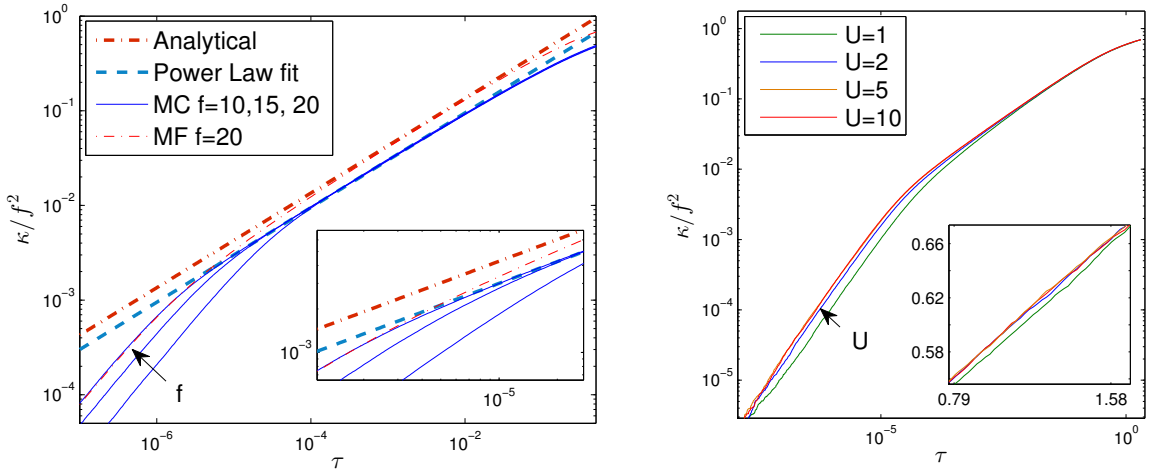

(a) (b)

Figure 8.7: (a) The local density fluctuations κ/f^2 as a function of τ, compared to a MF simulation [24] at $f = 20$. MC and MF are in agreement up to $\tau \sim 3 \cdot 10^{-6}$, where the MF drifts towards the analytical continuum result (5.9). Inset: zoom on the region where the MC and MF split. The MC follows the same power law as the one predicted in MF, although the prefactors are different. The MC result is also shown for fillings 10 and 15, where the same regime appears later in time. $U = 5$ ($L = 1000$ and 1100 runs for the MC). (b) The local density fluctuations plotted for several values of U at $f = 10$. Inset: zoom on the region around $\tau \sim 1$. We note that at f=10, the value of U only modifies the behavior at initial times, while all curves for $U \geq 2$ are similar in the sub-diffusive regime ($L = 10$ and 30000 runs).

In fig. 8.7 we show the local density fluctuations in the sub-diffusive regime, at different (high enough) fillings and interaction strengths. Fig. 8.7 (a) shows that the MF and MC simulations conform to a $\sim \tau^{1/2}$ power law, but that their pre-factors are different, due to the faster dynamics in MF (as explained in the last paragraph). Fig. 8.7 (b) shows that for $f = 10$, increasing the interaction strength from 1 to

10 only modifies the short term dynamics. For $U \geq 2$, the amplitude fluctuations are similar during the sub-diffusive regime. This can be understood in the expression for the rates in τ timescale. The hopping rate from a site with population n to a site with population m is given by (expressing U in units of Γ) $W_{nm} = \frac{f^2}{2} \frac{n(m+1)}{(n-m-1)^2+(1/U)^2}$. If $n \sim m$, this expression will be highly influenced by the value of U, due to the denominator ($W_{nn} = \frac{f^2}{2} \frac{n(n+1)}{1+(1/U)^2}$). If, however, as it will be at later times, neighboring sites start building large population differences, the denominator of W_{nm} will be dominated by the $(n-m-1)^2$ term. As a result, the choice of U will have little impact on the density fluctuation at long times.
We now consider two point correlations $C(d,\tau)$ (see fig. 8.8). Initially, $C(d,\tau=0) = 0$ since sites are entirely decorrelated. Then, correlations grow, and near neighbors are always more correlated than farther neighbors. We also observe that the correlations to neighbors at distances $d = 1$ through 6 all exhibit a power law behavior. The $C(d,\tau)$ curves show the same exponent $\sim \tau^{1/2}$ as we observed in the density fluctuations (see the inset in fig. 8.8 (a)). Furthermore, this behavior is reached for any high filling and high enough interaction strength (for example $f = 10$ and $U = 2$). At this point we may safely say that given f large enough, the dynamics at long times is not influenced much by the value of U (we will however verify this again in chap. 8.8).
Here we note that the sub-diffusive regime only appears for large enough fillings, as we have seen in the 2-site problem. The reason for that is that at low fillings the particle number boundary $n = 0$ is very quickly reached, which forces the system to extremely asymmetric configurations. At $f = 1$ for example, the system directly enters the last regime of relaxation towards the steady state once the initial linear regime is over.

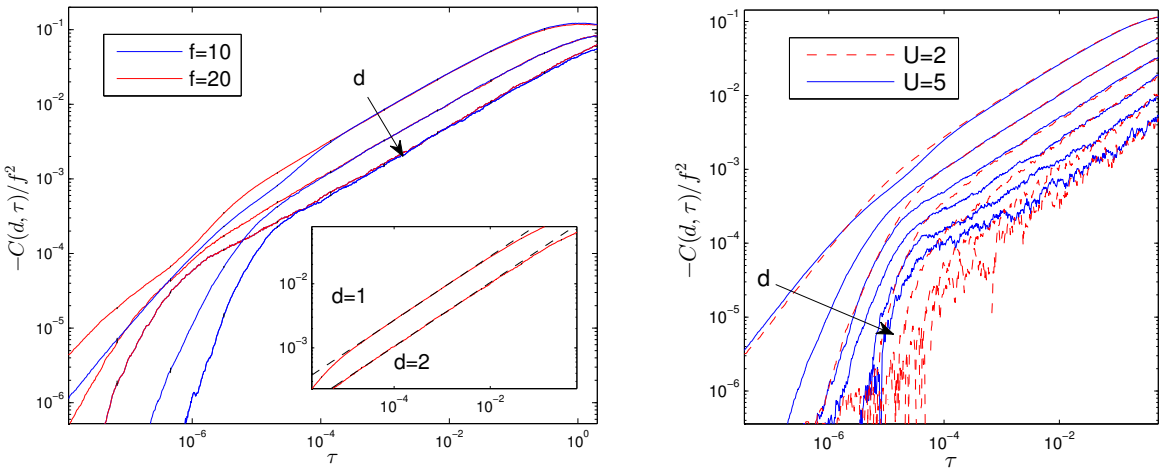

(a) (b)

Figure 8.8: (a) A plot of the density correlations at distances $d = 1$,2 and 3, for fillings $f = 10$ and 20, $U = 5$. Inset: zoom on the sub-diffusive regime for $d = 1$ and 2, along with a power law fit which suggests $C(1,\tau) \sim C(2,\tau) \sim \tau^{0.50\pm0.05}$. $U = 5$, $\Gamma = J = 1$, $L = 1000$, 1100 runs at $f = 10$, 100 runs at $f = 20$. (b) Density correlations up to distances $d = 6$, for $U = 2$ and 5. We note that the curves for different U come close together during the sub-diffusive regime. The large noise for large d values come from a small signal to noise ratio. Typically the error bars (a good estimator for curve fluctuations) are identical at all values of d.

8.5 Long term relaxation: finite systems at U=5

In the last sections we have never addressed the question of understanding how finite size effects affect the dynamics. In this section we will specifically study the long term relaxation of the system for finite systems, and along the way it will become clear that our previous results where not affected by finite size effects. All

fits shown here can be found in appendix A.
We have shown in sect. 3.1 that finite systems relax to a different steady state than the one for infinite systems. In fig. 8.1 (a) we plotted the spread of the ρ_n distribution for a system of length $L = 10$, and showed that the finite size distribution (3.5) is indeed reached. One can associate the last relaxation of the system (in red in fig. 8.1) with the final leveling off of the fluctuations (seen in fig. 8.1 (b)), as the system converges towards its steady state. An open question still remains however, and that is to understand when these finite size effects start, how they affect the dynamics, and what the evolution would be like if the system was not finite.

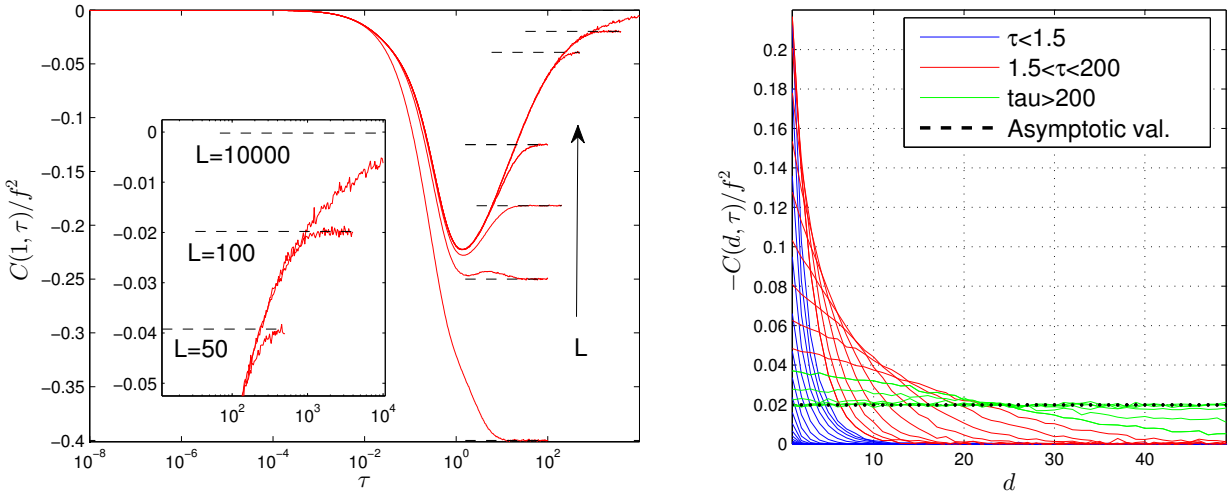

(a) (b)

Figure 8.9: (a) Density-density correlations between first neighbors versus rescaled time τ, plotted for several system lengths. The black dashed lines correspond to the resp. finite system asymptotic values (3.10). In the large system limit, there is a convergence towards a bell shape in the correlations. In shorter systems, the slow relaxation towards the infinite system steady state is interrupted by a fast relaxation towards the finite system steady state ($U = 5$ and $f = 1$). (b) Density correlations plotted versus distance, for rescaled times ranging from 10^{-8} to 3000, for a system with $L = 100$, $U = 5$ and $f = 1$. The three colors correspond to three different regimes in the spread of correlations, where we note the importance of finite size effects, see text for details. The number of computed runs range from: 700 at $L = 10000$ to $4 \cdot 10^6$ at $L = 10$. For $L = 100$, 150000 runs.

Power law spread of the correlations: To better understand system size dependence, we choose[1] to study a low filling system with $f = 1$ and relatively strong interactions $U = 5$. In fig. 8.9 (a) we plot the first neighbor correlations $C(1, \tau)$ as a function of rescaled time, for different system lengths. Initially, neighboring sites are uncorrelated, and the early dynamics lead to an increase of the correlations through particle exchanges[2]. As time advances, a crossover happens to the relaxation regime (around $\tau \sim 1.5$). In the large system limit, there is a clear convergence towards a bell-like shape in the correlations, as the system slowly relaxes to the uncorrelated infinite system steady state. In shorter systems, this slow relaxation is interrupted by a fast relaxation towards the finite system steady state value (3.10). Note here that this fast relaxation affects correlations at all distances. Fig. 8.10 (a) for example plots the behavior of $C(d, \tau)$ to all

[1] for computational reasons

[2] If the filling was higher this would correspond to the linear regime followed the sub-diffusive regime. At $f = 1$, the linear regime is directly followed by the relaxation to the steady state

distances in a system of length $L = 100$ ($C(d, \tau)$ elements are symmetric around $d = 50$ for $L = 100$, so only the first 50 are plotted). There we see that beyond $\tau \sim 200$, all correlations converge towards the finite system's value.
The start of the finite system relaxation can be associated with the moment where correlations rise at a distance $d = L/2$. This is seen in fig. 8.10 (a), but also in fig. 8.9 (b), where we plot the distribution of the correlations for different times. There it becomes clear that beyond a certain time ($\tau \sim 200$ for $L = 100$), all sites in the chain become correlated, and the fast relaxation to the finite system steady state equates to a leveling out of these correlations throughout the chain.
To best quantify the moment where correlations become important on a system scale, it appears of importance to define a form of 'correlation length'. In the following we will use a crude definition that proves simple to implement, yet yields interesting results. We define $d(\tau)$ as the length at which:

$$|C(d(\tau), \tau)| \geq 0.005 \tag{8.2}$$

i.e. given a time τ, $d(\tau)$ is the distance where correlations reach or exceed the arbitrary threshold value of 0.005. If this threshold is chosen too low, the resulting observable will be subject to noise. If it is chosen too high, we might miss the moment where the correlations reach half the chain length. This threshold is illustrated in fig. 8.10 (a), and the resulting curve is shown in fig. 8.10 (b). Interestingly, $d(\tau)$ shows a power law behavior $\tau^{0.38\pm0.2}$ once the peak in the first neighbor correlations is passed (for $\tau > 1.5$), and flattens out once half the system length is reached. This power law can be used to extrapolate the moment when finite size effects are to be expected for any system length (fig. 8.10 (b) inset).

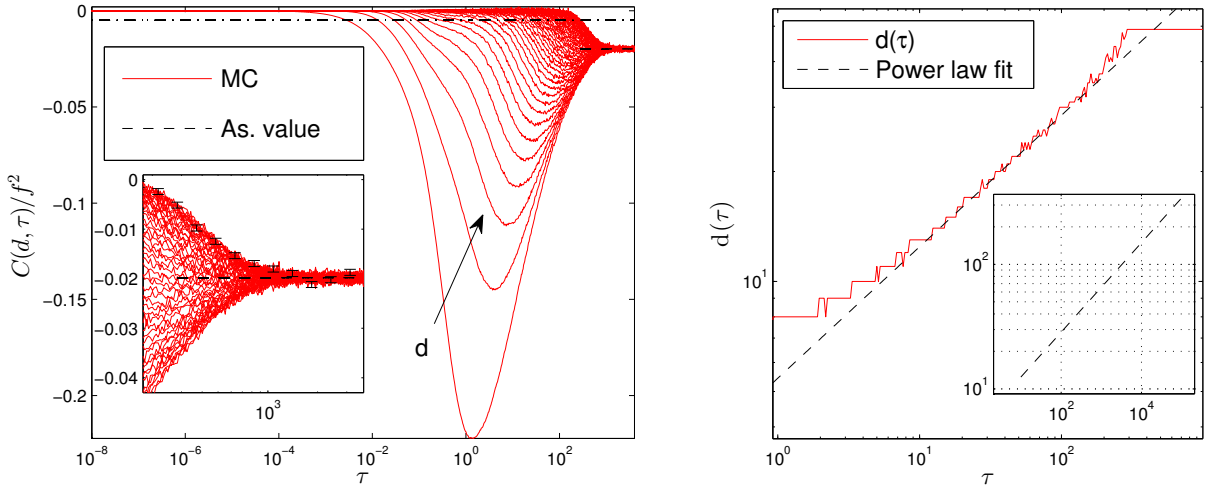

(a) (b)

Figure 8.10: (a) Plot of the density correlations versus rescaled time, for a system of length $L = 100$. We note the relaxation of the correlations towards the finite system value (shown in black dashed lines), magnified in the inset (error bars are shown for $d = 50$). (b) Plot of the correlation length defined in (8.2), along with a power law fit. An extrapolation up to $\tau = 10^5$ is shown in the inset. $f = 1$, $U = 5$.

Finite system stretched exponential relaxation: Now that we understand why and when finite size effects arise, we will characterize their effect on the system. For this we will analyze the density fluctuations. In fig. 8.11 we plot the density fluctuations for $f = 1$ and $U = 5$ for various system lengths. Again we see that in the infinite system limit the fluctuations have a slow relaxation towards the infinite system fluctuation value κ_∞ (3.9), while finite system constraints force the system to a fast relaxation towards κ_∞^L. In

fig. 8.12 we plot $1 - \kappa/\kappa_\infty^L$ versus $\sqrt{\tau}$ for several filling values at $L = 10$, and at $f = 1$ for various system sizes. Presented in this way, the fast relaxation towards the finite system steady state exhibits a stretched exponential behavior for short systems. Unfortunately, since this final decay is fast, and only happens close to the asymptotic value, it is hard to observe this regime over a long period of time. At $L = 10$ and $f = 10$ for example, the stretched exponential is seen from rescaled times $\tau \approx 6$ to $\tau \approx 20$, where a very poor signal to noise ratio render the curve useless. In contrast, the relaxation of an $L = 10000$ system towards its steady state (at $L = 10000$ and $f = 1$, $\kappa_\infty^L = 1.9996 \approx 2 = \kappa_\infty$) does not exhibit any stretched exponential decay within the reached timescale, and is less subject to noise due to the slower convergence. This slow decay towards the infinite system steady state will be further studied in the following sections.
At this stage the question naturally arises: why should a finite system relax towards its steady state in the same way than mean field systems relax towards the infinite system steady state? In the MF description, the stretched exponential arose due to rare events in the tail of the e^{-x} distribution. These events where identified as the formation of large piles, which then dominated the time evolution. A possible explanation for the stretched exponential behavior in the MC description for finite systems is based on the spreading behavior of the correlations. Say the correlation length reaches half the system length after a time $\tau = 1$. This means that any 2 sites have been allowed to exchange atoms in a duration $\Delta\tau = 1$. If we now look at the system on a timescale Δt, coarse graining turns our system into a system where all sites are allowed to communicate within a time step. Large piles naturally retain a slow evolution, but the rapid movements of smaller piles are averaged out over chain. In this perspective, a behavior close to the one described in mean-field can be conceived. It can therefore seem reasonable for a finite system to decay in a stretched exponential fashion.

Finite system vs. infinite system relaxation
To illustrate the differences between a finite and infinite system relaxation, we can compare density plots of the atom population on each site, in a single run, for two different system lengths. This comparison is shown in fig. 8.13 for a system of length 10 and a system of length 50. Plots range from rescaled times $\tau = 1$ (roughly the moment where the correlation length reaches 5) to $\tau = 40$ (still before the moment where finite size effects affect the $L = 50$ system). These plots are by no means representative of the rich dynamics of the system, but we may use them for qualitative intuition. We note that in the $L = 10$ system, there is only a single high pile a time. Its appearance usually holds out over 5 units of rescaled time, while we notice faster movements in smaller piles. In contrast, in the $L = 50$ system, we note that several high piles can appear simultaneously, and that these remain roughly 5 to 10 sites apart (approximately the correlation length). On a longer timescale, higher piles tend to be farther and farther apart. This perspective brings us to another possible qualitative interpretation.
It would seem like the system forms clusters, roughly the size of the correlation length. Let us consider a given time τ_0, and its correlation length $d(\tau_0)$. In the evolution from τ_0 to $2\tau_0$, the correlation length implies that particles can be exchanged between all sites in the cluster, and we could locally expect a rapid convergence to the steady state in τ_0 scale, as mentioned in the last paragraph. In this evolution, the buildup of large piles is associated with depletion of

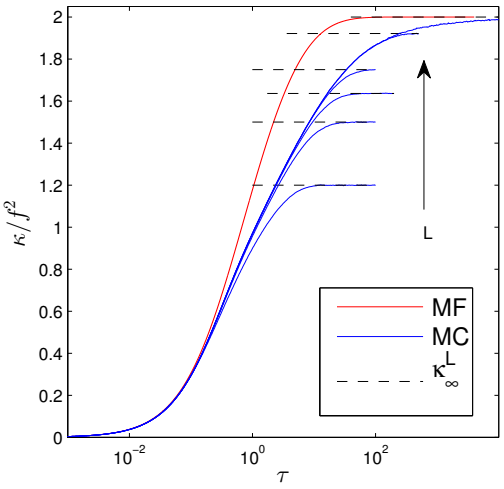

(a)

Figure 8.11: The density correlations plotted for $f = 1$, $U = 5$, for system sizes $L = 4, 7, 10, 15, 50, 10000$. The MF counterpart [24] is also shown along with the asymptotic fluctuation values for all system sizes. In the large system limit, a slow convergence of κ towards κ_∞ is observed, while finite systems and the MF simulation relax quickly towards their respective steady states.

the sites in the cluster. As the cluster size grows, inter-pile distances should also grow. These qualitative observations need to be confirmed by more detailed analysis.

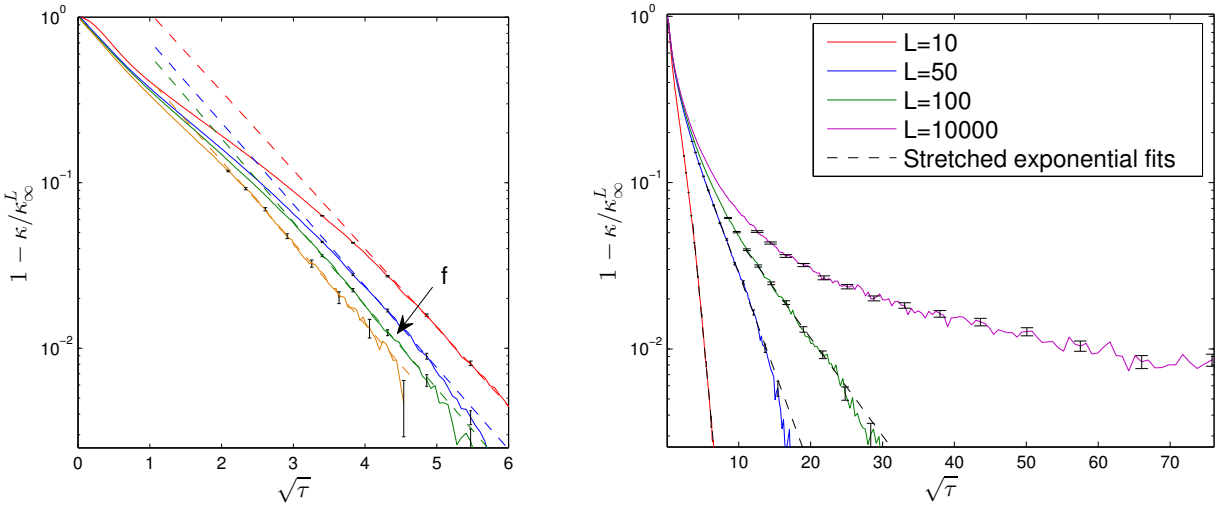

(a) (b)

Figure 8.12: Plots of the relaxation towards the finite system steady state. (a): $L = 10$ and $f = 1, 2, 3, 10$. (b): $f = 1$ and $L = 10, 50, 100, 10000$. For small systems we note a stretched exponential behavior (see fits in dashed lines), which is not seen for $L = 10000$ within the reached time.

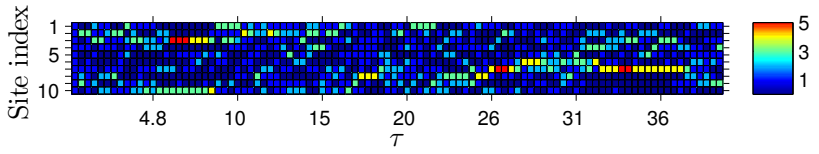

(a) $L = 10$

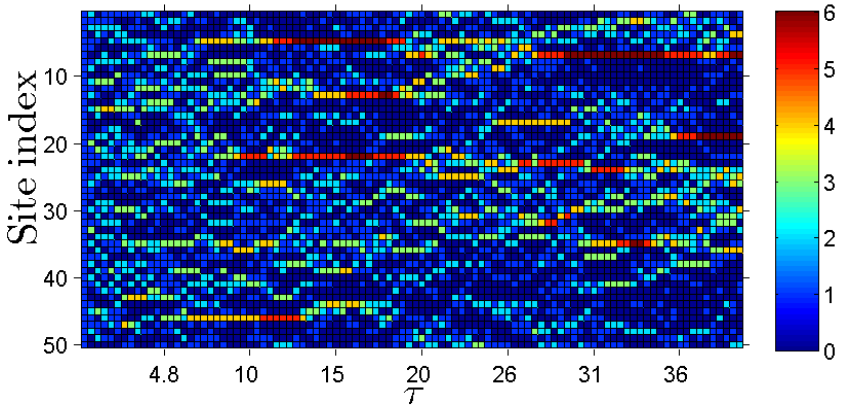

(b) $L = 50$

Figure 8.13: Density plots of the system state at $\Delta\tau = 0.5$ intervals. The color map indexes the atom number on each site. (a) $L = 10$, $f = 1$, $U = 5$ and (b) $L = 50$, $f = 1$, $U = 5$. In (a), finite size relaxation is on march, while (b) is still representative of a infinite system relaxation. See text for details.

8.6 Long term relaxation: low filling, weakly interacting limit f=1, U=1

In the last section, we have shown that in the infinite system size limit, a decay slower than a stretched exponential is to be expected both in the correlations and in the fluctuations. We will show here that this decay is a power law, which comes from very different physics than the one leading to the stretched exponential in the MF description.
As seen in fig. 8.14, the final decay is characterized by an ongoing spread of correlations, which also become smaller within the $d(\tau)$ domain as time advances. In this section we have chosen a low filling weakly interacting limit $f = 1$, $U = 1$ to start our study of the long-term decay of the system. In this limit, we where able to run simulations with $L = 10000$ up to rescaled times of $\tau = 10^5$, times where the system gets close to its steady state (see fig 8.14 (b)). For such long systems, we have ruled out finite size effects (the correlation spread analysis, see last section) and the ρ_n elements converge towards a distribution very close to the infinite system steady state, as we can see in fig. 8.15 (a). At this point it appears of importance to identify which features of our system can truly be traced back to the anomalous transition rates. In fact, we will see that another system, the N-body random walk, exhibits a lot of the characteristics we could have associated with the anomalous diffusion. In the N-body random walk, $N = fL$ particles are first evenly distributed over the L sites, and these evolve with a simple rule: each particle has a constant factor D as its left/right hopping rate. In our L site density matrix formulation, this equates to replacing the N body rates (3.13) by $W_{nm} = nD$.

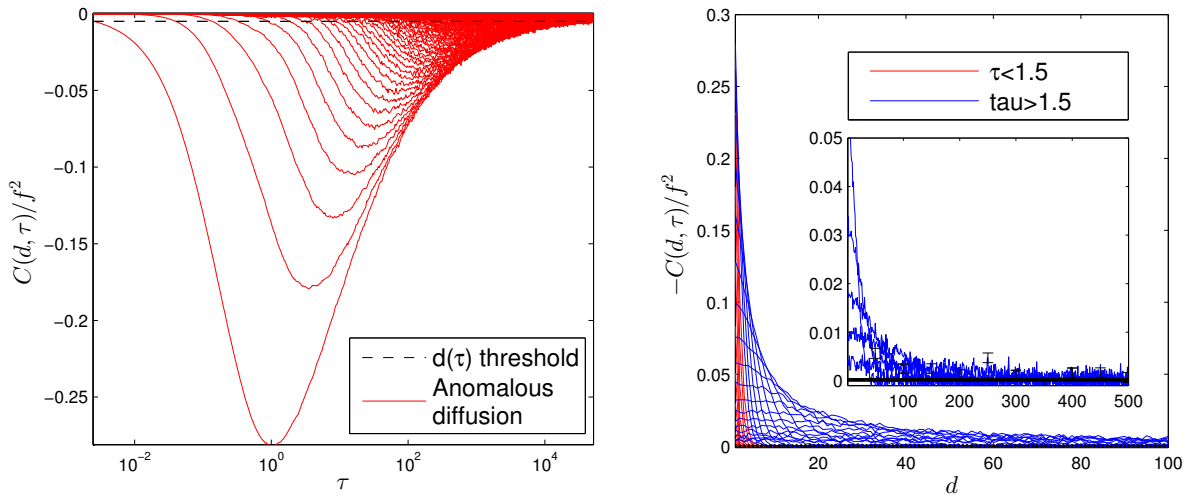

(a) (b)

Figure 8.14: (a) Plot of the correlations versus rescaled time up to length $d = 500$ in a system unaffected by finite size effects. (b) The correlation distribution for rescaled times ranging from 10^{-8} to 10^5. $\tau \approx 1.5$ marks the crossover to the final relaxation. Inset: Correlation up to distance $d = 500$, for times $\tau > 200$. Error bars are shown for the final time distribution $\tau = 10^5$. $L = 10000$, $f = 1$, $U = 1$, 700 runs.

In the N-body random walk, there is no process favoring the buildup of large piles, and so we would expect the steady state distribution of the ρ_n elements to be narrower than the one with the anomalous rates. This comparison in done in fig. 8.15, where we clearly see that the RW never reaches the maximal entropy state.

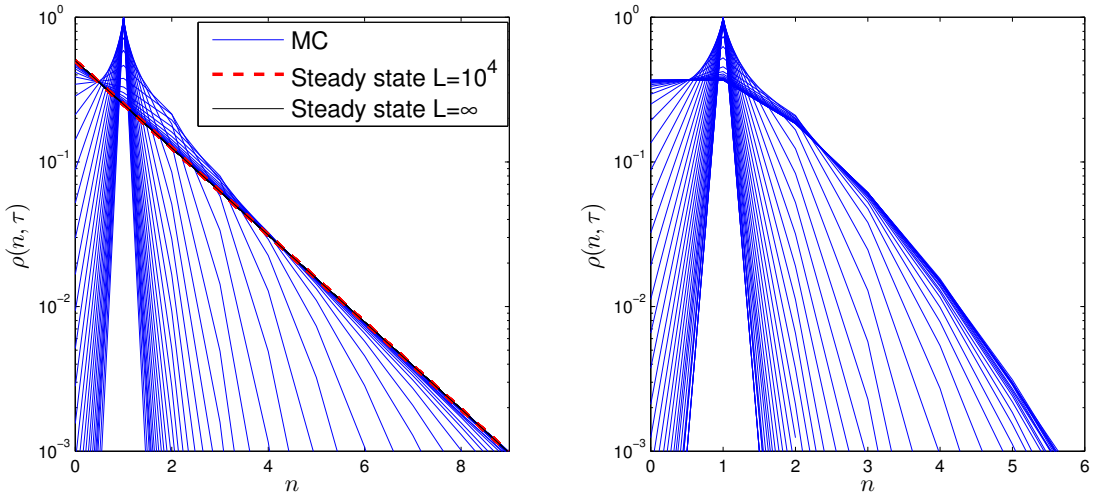

(a) Anomalous diffusion

(b) N-Body random walk

Figure 8.15: Denstiy matrix element distribution at times ranging from 10^{-8} to 10^{5}, comparing a N-body random walk (b) to the random walk with anomalous factors (a). Note that the random walk does not reach the maximum entropy state.

However, when we plot the density-density correlations for the RW, we first notice that these are qualitatively very much the same than the ones obtained from the $f = 1$ and $U = 1$ system. Due to the absence of interactions, the sub-diffusive regime does not appear, but the initial linear regime is to be recognized, and the peak in the correlations as a function of time also occurs (see fig. 8.16(a)). Furthermore, the long term relaxation towards the steady state can be identified as a power law $\tau^{-1/2}$ both for the RW and the $f = 1$, $U = 1$ system. The correlation length can be determined for the two systems, and yields the same $\sim \tau^{0.38}$ power law as mentioned in the previous section for a $f = 1$, $U = 5$ system. The local density fluctuations of the two systems relax to their resp. steady states following a $\tau^{-1/2}$ decay.
This comparison to the N-Body random walk shows that not all features of the dynamics are characteristic of our system. For example, the first neighbor correlation increase and then decrease is not related to the anomalous rates. While at short times correlations grow due to events linking neighboring sites, these correlations decay again due to the transition to a fully random configuration.
The $1/\sqrt{\tau}$ power law decay of the correlations and the fluctuations also isn't specific to our system. In the random walk, higher entropy states are only reached by coincidence of particles on the same sites, rather than by intricate dynamics between neighboring sites. The origin of the power law behavior should therefore be searched for in a global behavior of the system.
Here we could postulate that the correlation length plays a key role in the final relaxation. Since the decay of the density fluctuations follows a power law, it may just come from the power law spread of the correlations. In the last section we have proposed that the system adopts a behavior close to mean field within the correlation length. In this sense, we could locally (within a cluster) expect a fast relaxation towards the maximum entropy configuration. On a longer timescale, within a cluster, we could therefore locally expect maximal entropy. As time advances, this entropy then slowly extends to the whole chain as the correlation length grows. Here we could say that the slow spread of the correlations impedes the spread of entropy. Unfortunately we do not have the right observables at hand to confirm this.

8.7 Long term relaxation: effect of interactions in the low filling limit f=1

In the last section, we have seen that the long term relaxation of a system unaffected by finite size effects generally followed a power law. We have shown the the spread of the correlations also followed a power law and that these power law behaviors where also found in an N-Body random walk with constant rates. In this section we will show that this behavior is also found in systems with higher interaction strengths. All fits shown here can be found in appendix A.

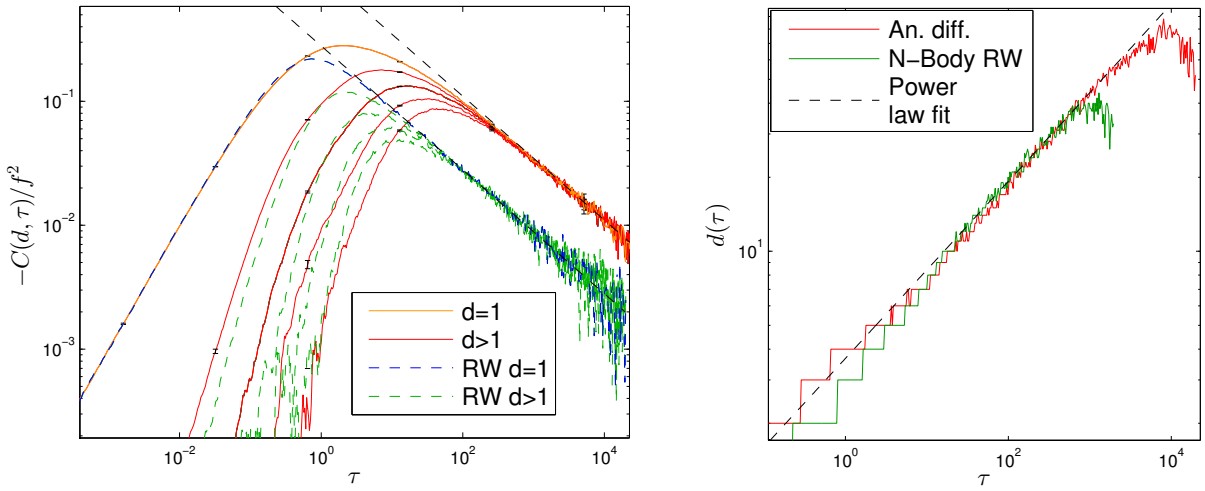

Figure 8.16: Comparison of normal (RW) and anomalous diffusion (An. diff.) rates in a N-particle random walk. (a) Plot of the density correlations versus rescaled time for $d = 1$ to 5. In both cases the final relaxation follows a $\sim \tau^{-1/2}$ power law. (b) Plot of the correlation length, which follows a $\tau^{0.38\pm0.02}$ power law. Note that although correlations keep spreading in the chain, $d(\tau)$ starts diminishing beyond a certain time. This artifact comes from the fact that, beyond a a certain time, the value of the correlations become smaller than the threshold. (c) Plot of the relaxation of the local density fluctuations towards the respective asymptotic values. This final relaxation follows a $\tau^{-1/2}$ power law.

In fig. 8.17 we plot the decay of the density fluctuations at $f = 1$ for $U = 1, 2, 5, 10$. We note that all

curves follow a power law and that the pitch grows as the interaction strength is increased (see appendix A for the exact values). Most interestingly, we also see that above $\tau \approx 1000$, the fluctuations enter another regime, where the decay follows $\sim \tau^{-0.5}$, as in the random walk. This is well seen at $U = 5$ (8.17(b) and inset, green curve).

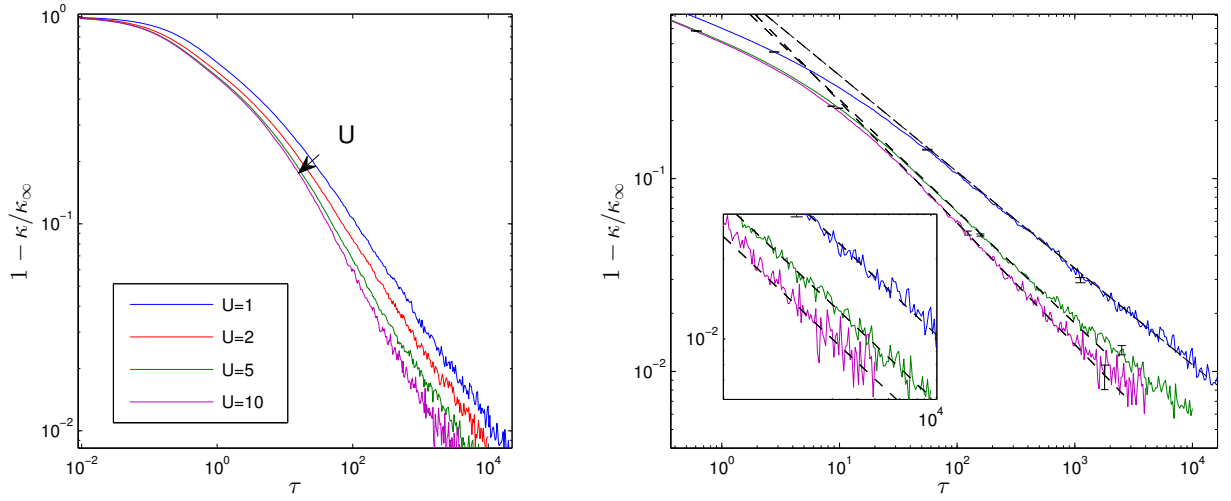

(a) (b)

Figure 8.17: (a) Relaxation of the local density fluctuations at $f = 1$, for various interaction strengths. (b) Same as in (a) but including power law fits. Inset: Final part of the relaxation regime, along with $\sim \tau^{-1/2}$ lines (black dashed). At higher interaction strengths, 2 regimes seem to appear, a first $\tau^{-\alpha}$ regime with $\alpha > 1/2$ followed by another regime with $\alpha = 1/2$ (for exact α values see appendix A).

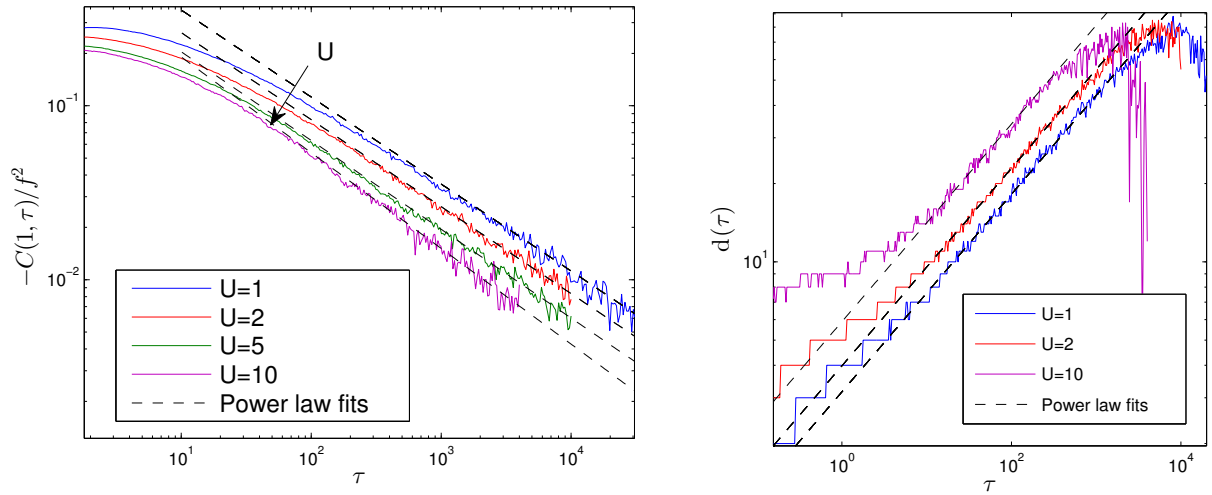

(a) (b)

Figure 8.18: (a) Relaxation of the $d = 1$ density-density correlations at $f = 1$, for various interaction strengths, along with power law fits. A slight drift of the slope is to be observed. (b) Plot of the correlation length $d(\tau)$ versus rescaled time τ, along with power law fits. All slopes are found in appendix A $L = 10000$

When studying the first neighbor correlations, fig. 8.18(a) shows that power laws also appear in the final decay, and that there is also a slight evolution of the slope as U is increased. The correlation length

(fig. 8.18(b)) as a function of τ shows the same $\tau^{0.38\pm0.02}$ power law for all values of U. Noise does however not allow us to look at $d(\tau)$ very far in time, and an eventual drift of the slope cannot be excluded.

8.8 Long term relaxation: effect of interactions in a system with high filling f=10

The last few sections have pointed out the power law behavior of the decay towards the steady state in a dilute system at $f = 1$. In this section, we investigate the final decay of unconstrained systems for high fillings[3]. Simulations run up to time $\tau = 400$ where the beginning of the power law regime is visible. All fits shown here can be found in appendix A.

In fig. 8.19 we plot the first neighbor correlations and the local density fluctuations for $U = 2$ and $U = 4$. In both cases power laws slightly different from the ones at $U = 1$ are to be recognized: $\kappa/f^2 \sim \tau^{-0.54\pm0.02}$ and $C(1,\tau) \sim \tau^{-0.47\pm0.02}$. The increase of U from 2 to 4 does not seem to significantly alter the dynamics, and we do not expect even higher interactions to alter this behavior. The correlation length spreads in a $\sim \tau^{0.38}$ power law, as in the $U = 1$ system (see fig. 8.19(b) inset).

These simulations show that very little is still understood about the system's long-term infinite-L relaxation. Beside a slight drift in the exponent of the power laws, all the considered observables qualitatively behave as in a random walk. This observation has been made for several interaction strengths, and holds out at large fillings. Although we could have expected such a behavior for weak interactions (in the sense that interactions may be neglected), the fact that this holds out in the large filling and large interaction limit is rather astonishing. In further investigations, the N-particle random walk first needs to be better understood, before understanding the drift of the exponents due to interactions.

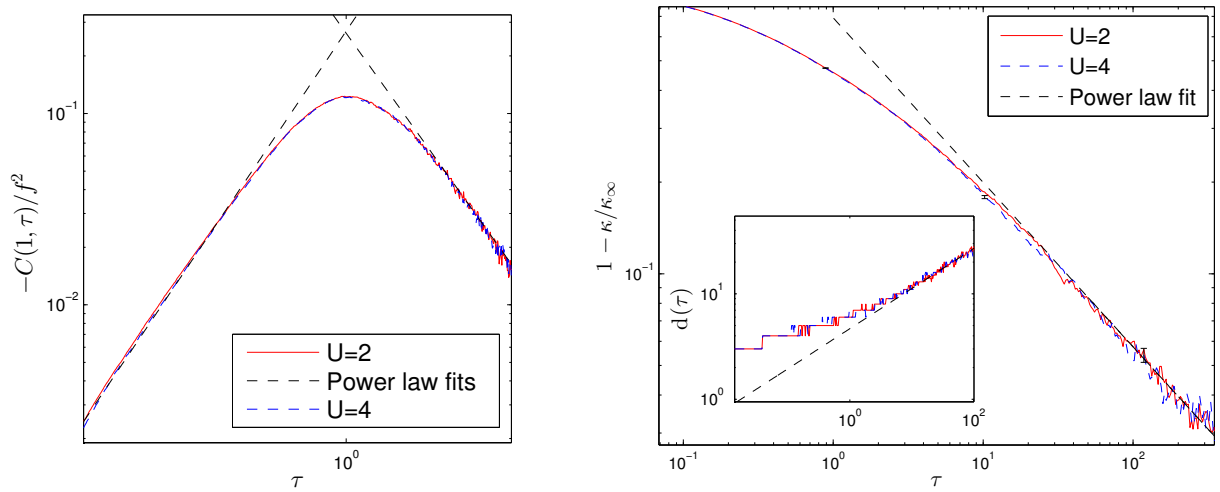

(a) (b)

Figure 8.19: (a) Plot of the local density fluctuations at $f = 10$ for $U = 2$ and $U = 4$. We note the power law of the sub-diffusive regime ($\sim \tau^{1/2}$), and the power law of the relaxation ($\sim \tau^{-0.47}$). (b) Plot of the local density fluctuations versus rescaled time, along with a $\tau^{-0.54}$ power law fit. Note that there is no significant change in the effect of U on the system above $U = 2$. Inset: Plot of the correlation length versus rescaled time for $f = 10$, along with a $\sim \tau^{0.38}$ power law fit. $L = 3000$ apart from $U = 1$ where $L = 10000$. No finite size effects are to be expected in the shown times.

[3]For computational reasons, we have limited the final simulation time (simulations go up to $\tau = 400$), and reduced the system length ($L = 3000$ should still not shown finite size effects at $\tau = 400$).

CHAPTER 9

Summary and outlook

To summarize, we have shown that in the Bose-Hubbard model coupled to a dissipative environment, several dynamical regimes appear. On time scales larger than the one associated with the coupling strength, the joint action of dissipation and tunneling energy makes atoms jump around the lattice. As the system is forced into configurations otherwise disfavored by interactions, the total energy of the system rises. In the early dynamics, single particle events lead to a linear rise of the system energy. As time evolves, at large enough lattice fillings, a sub-diffusive power law regime appears, due to the complex interplay of atom pileups. In the long term evolution, finite size effects play a major role in the dynamics. While short systems exhibit a stretched exponential decay towards the maximum entropy state, infinite systems relax as a power law.

The use of a rejection free Monte-Carlo algorithm has allowed us to gain insight in a system previously only understood within mean-field approaches. In the sub-diffusive regime, simulations have allowed us to confirm the critical exponent predicted in previous works. In the long term evolution however, the final relaxation of the system towards the steady state is yet to be fully understood. Surprisingly, we have uncovered that the finite size system relaxation is similar to the mean-field picture for infinite systems, and that the infinite size system relaxation resembles the one observed in a random walk of non-interacting particles.

A possible explanation for the behaviors observed at long times is associated with the growing of a characteristic length scale in the density-density correlations, but further investigation is clearly needed there. Additional work on the subject could target a full understanding of the decay of correlations in a random walk, before studying the influence of interactions. As new analytical calculations could be developed (to extend mean-field and include the dynamics of correlations), numerical study of the system can evolve around other forms of correlation. Time correlations and higher order correlations would for example be most helpful to better understand the physics.

I would like to thank Corinna Kollath for granting me the opportunity to work on this project within her group, as well as for her invaluable help. This project has introduced me to the very stimulating work in a research group, as well as the thrilling many-body physics encountered in ultracold gases. I would like to thank Bruno Sciolla and Dario Poletti for their numerous, helpful and motivating discussions, as well as Anabel Chuinard, Peter Barmettler and Emanuele Coira.

APPENDIX A

Exact fit parameters, long term relaxation

In this section we show the exact values of the fitting parameters for the fits shown in sections 8.6 and following. These summarize the behavior of the final power law relaxation observed in large systems. Although numerical fitting routines where used, numerically obtained error estimates where adjusted qualitatively by agreement to the eye.

Configuration	κ powerlaw	$C(1,\tau)$ powerlaw	$d(\tau)$ Powerlaw
$f=1$, $U=1$	$\tau^{-0.50\pm0.01}\cdot 10^{0.035\pm0.005}$	$\tau^{-0.50\pm0.02}\cdot 10^{0.05\pm0.02}$	$\tau^{0.38\pm0.02}\cdot 10^{0.5\pm0.05}$
RW $D=1/2$	$\tau^{-0.50\pm0.02}\cdot 10^{-0.55\pm0.05}$	$\tau^{-0.50\pm0.02}\cdot 10^{-0.55\pm0.05}$	$\tau^{0.38\pm0.02}\cdot 10^{0.5\pm0.05}$
$f=1$, $U=5$	$\tau^{-0.58\pm0.01}\cdot 10^{-0.01\pm0.01}$	$\tau^{-0.51\pm0.02}\cdot 10^{-0.18\pm0.01}$	$\tau^{0.38\pm0.02}\cdot 10^{0.6\pm0.05}$
$f=1$, $U=10$	$\tau^{-0.63\pm0.01}\cdot 10^{0.03\pm0.02}$	$\tau^{-0.55\pm0.02}\cdot 10^{-0.17\pm0.02}$	$\tau^{0.38\pm0.02}\cdot 10^{0.77\pm0.05}$
$f=10$, $U=2,4$	$\tau^{-0.54\pm0.02}\cdot 10^{-0.16\pm0.02}$	$\tau^{-0.47\pm0.02}\cdot 10^{-0.58\pm0.02}$	$\tau^{0.38\pm0.02}\cdot 10^{0.67\pm0.03}$

APPENDIX B

About the code

In this work, all codes where written in Matlab®, using the 2010a edition. All plots shown in this report have been obtained by the code shown hereafter or slight variations of it. The code was designed to run in parallel on Perseus, a 504-core cluster used by the Department of Theoretical Physics at the University of Geneva. The cluster's 42 nodes each account 35Gb's of RAM, and host 12 1.6 Ghz Cpu's. The code was also designed to take advantage of the very efficient vector/matrix operations in Matlab, and the use of functions minimized for optimal performance (since it is a non-compiled language, repeated function calls tend to dramatically slow down computations).
In a simulation, each node receives the system parameters and a number of runs to execute. During the Monte-Carlo main loop, observables are not computed, only the system state (the $\mathbf{n}$ vector) is written down for each required time point. Once the simulation is done, each node then bulk computes the observables for its runs and writes them to a file (as many data files as involved nodes are written). To obtain the final observables, a final summation is done by combining all the data files. The code to collect the data was written so that data with different numbers of runs could be combined (this allows to add data files to an already executed simulation, and is the reason for the compensation factor seen in the code).
Typical runs shown in the different plots have a 1-day runtime: For short system lengths ($L \sim 10$), convergence towards the steady state is quick, but up to 10^6 runs have to be done to obtain decent statistics. In this procedure care needs to be applied not to exceed RAM constraints. In long systems ($L \sim 10000$), fewer runs need to be done since the average over sites already produces considerable statistics. However, reaching the system steady state reveals to be a lengthy procedure (at $L = 10000$, $f = 1$, $U = 1$, it takes a node up to 30 hours to reach $\tau = 10^5$ once).
To be used, the code first needs to be compiled and then executed using a shell script. When compiling the code, Matlab generates a script to setup the environment variables and launch the executable. This generated script is the one that is executed by our command script (see Main code: shell script below). In the command script, all system parameters are set, and the matlab generated script is distributed to a given number of nodes.

Main code: shell script

```
#!/bin/bash
#$ -S /bin/bash
#$ -cwd
#$ -t 1-100      # distributes the code to 100 nodes
```

```
f=1
L=15
U=5
Gamma=1
J=1
Runs=10000
taui=0.00000001
tauf=20
Tpoints=1000
Num_files=100
coll_rho=0
dmax=10

export OMP_NUM_THREADS=1

./MainMCV12_run.sh $HOME/MCR/v713 ${SGE_TASK_ID} $f $L $U $Gamma $J $Runs $taui $tauf
$Tpoints $Num_files $coll_rho $dmax
```

Main code:

```
function MainMCV12_3(id,f,L,U,Gamma,J,Runs,taui,tauf,Tpoints,Num_files,coll_rho,dmax,Nmax)
%%%%%%%%%%%%%%%%%%%%%%%%%%%%%%%%%%%%%%%%%%%%%%%%%%%%%%%%%%%%%%%%%%%%%%%%%%%%%%%
% KMC to sample a master equation's evolution
% This code should be distributed over several cores in a simulation
% Function call: MainMCV12(id,f,L,U,Gamma,J,Runs,taui,tauf,Tpoints,Num_files,coll_rho)
% id: index of the code launch
% f:Chain filling
% L: number of sites
% U: Interacion parameter
% Gamma: Dissipation parameter
% J: Hopping parameter
% Runs: Number of runs to be done by this code
% taui: initial rescaled time
% tauf: final rescaled time
% Tpoints: number of measurement points
% Num_files: number of parallel processes
% coll_rho: Choose whether rho should be calculated (Very time-consuming)
% dmax: Maximum distance to which correlations should be computed\..
\.. (limited to chain length)
% Nmax: Maximum atom number for which rho should be computed
%
% Output is saved to a folder named after the input and contains:
%  -Raw data files: Raw observables summed over node's runs, and their error.
%  -Output text file, stores start time of each node, seeds, simulation
%   parameters and running time.
% Remarks:
%  -Time points are distributed logarithmically within the given limits
%  -Known issue to improve: when launching very short simulations, several
%  nodes might try opening output text file at the same time, leading to
%  some missing output in the file.
%%%%%%%%%%%%%%%%%%%%%%%%%%%%%%%%%%%%%%%%%%%%%%%%%%%%%%%%%%%%%%%%%%%%%%%%%%%%%%%

%%%%%%%%%%%%%% Convert all input parameters (from shell script) to numbers
```

```
id=str2num(id);
f=str2num(f);
L=str2num(L);
U=str2num(U);
Gamma=str2num(Gamma);
J=str2num(J);
Runs=str2num(Runs);
taui=str2num(taui);
tauf=str2num(tauf);
Tpoints=str2num(Tpoints);
Num_files=str2num(Num_files);
dmax=str2num(dmax);
Nmax=str2num(Nmax);

%%%%%%%%%%%%%% Initial condition and simulation parameters
N=f*L; % Total number of atoms
Nruns=Runs*Num_files; % Total number of runs
n0=ones(L,1)*f; % Initial chain configuration

%%%%%%%%%%% Define time grid
Ti=taui/(4*Gamma*J^2/(f^2*U^2));
Tf=tauf/(4*Gamma*J^2/(f^2*U^2));
taui=Ti*4*Gamma*J^2/(f^2*U^2);
tauf=Tf*4*Gamma*J^2/(f^2*U^2);
T=logspace(log10(Ti),log10(Tf),Tpoints);

%%%%%%%%%%%%%%%%%%%%%%%%%%%%%%%%%% Setup random generator
newseed=sum(100*clock)+id;
if (newseed>2^23)
newseed=newseed-2*id;
end
RandStream.setDefaultStream(RandStream('mt19937ar','seed',newseed))

%%%%%%%%%%%%%%%%%%%%%%%%%%%%%%%%%% Setup output, output parameters
name=['L',num2str(L),'f',num2str(f),'U',num2str(U),'Gamma'\..
\..,num2str(Gamma),'J',num2str(J),'tauf',num2str(tauf)];
cdir=pwd;
mkdir(cdir,name)
OUTname=([name,'/',name,'OUT.txt']);
format shortg
c = clock;
fid = fopen(OUTname,'a');
fprintf(fid,['ID: ',num2str(id), ' Seed:',num2str(newseed),', Launch \..
\.. time (y/m/d/h/m/s): ',num2str(c),'\r']);
fclose(fid);

tic
%%%%%%%%%%%%%% Measurement initializations
navg_RAW=zeros(L,Tpoints);     % Avg particle number
kavgL_RAW=zeros(1,Tpoints);            % Fluctuation
kavgL_err_RAW=zeros(1,Tpoints);
```

```
dmax=min(floor(L),dmax);
densavgL_RAW=zeros(Tpoints,dmax);     % Correlations
densavgL_err_RAW=zeros(Tpoints,dmax);
if (coll_rho=='1')
PnavgL_RAW=zeros(Tpoints,Nmax+1);                                % Density matrix elements
end

%%%%%%%%%%%%%% main loop over runs
    MCout=zeros(L,Tpoints,Runs);     % Will contain system state at the given time points
    factor=2*(J/U)^2*Gamma;

    for run=1:Runs
        n=n0;
        W=zeros(2*L,1);
        WL=zeros(L,1);
        WR=zeros(L,1);
        nm1=circshift(n,[1,0]);
        np1=circshift(n,[-1,0]);
        WL=factor*n.*(nm1+1)./( (n-nm1-1).^2 +(Gamma/U)^2 );
        WR=factor*n.*(np1+1)./( (n-np1-1).^2 +(Gamma/U)^2 );
        %WR(L)=0; % Uncomment to get fixed boundary conditions
        %WL(1)=0; % Uncomment to get fixed boundary conditions
        W=[WL;WR];
        C=cumsum(W);

        t=0;
        Tlast=0;
        flag=1;
        while flag
            Wtot=C(2*L);
            tau=-(1.0)/Wtot*log(rand);
            t=t+tau;                                                    %Increment time
            %%%%%%%%%%%%%%%%%% measurement & exit condition
            while(Tlast<Tpoints  && t>T(Tlast+1))
                MCout(:,Tlast+1,run)=n;
                Tlast=Tlast+1;
            end
            if (Tlast+1)>Tpoints                                %Main MC loop exit condition
                flag=0;
                break
            end

            %%%%%%%%%%%%%%%%%% Binary search for new config
            value=(rand)*Wtot;
            low = 1;
            high = length(C) - 1;
            while( low <= high )
                j = ceil((low + high)/2);

                if( C(j) > value )
                    high = j - 1;
```

```
                elseif( C(j) < value )
                    low = j + 1;
                else
                    if(C(j)~=C(j-1))
                        high=low;
                    end
                    high = j - 1;
                end
            end
            j = low;

            %%%%%%%%%%%%%%%%%% Find the corresponding site indexes
            q=mod(j-1,L)+1; % Starting site

            if j>L % Hopping executed to the right
                qnext=mod(q+1-1,L)+1; % Target site
                qR=  mod([q-1,q  ,q+1]-1,L)+1; % Sites where hopping to the right is\..
\.. to be updated
                qRp1=mod([q  ,q+1,q+2]-1,L)+1;
                qL=  mod([q  ,q+1,q+2]-1,L)+1; % Sites where hopping to the Left is\..
\.. to be updated
                qLm1=mod([q-1,q  ,q+1]-1,L)+1;
            else % Hopping executed to the left
                qnext=mod(q-1-1,L)+1;
                qR=  mod([q-2,q-1,q  ]-1,L)+1;
                qRp1=mod([q-1,q  ,q+1]-1,L)+1;
                qL=  mod([q-1,q  ,q+1]-1,L)+1;
                qLm1=mod([q-2,q-1,q  ]-1,L)+1;
            end

    % Update system
            n(q)=n(q)-1;
            n(qnext)=n(qnext)+1;
            WL(qL)=factor*n(qL).*(n(qLm1)+1)./( (n(qL)-n(qLm1)-1).^2 +(Gamma/U)^2 );
            WR(qR)=factor*n(qR).*(n(qRp1)+1)./( (n(qR)-n(qRp1)-1).^2 +(Gamma/U)^2 );
            %WR(L)=0; % Uncomment to get fixed boundary conditions
            %WL(1)=0; % Uncomment to get fixed boundary conditions
            W=[WL;WR];
            C=cumsum(W);
        end
    end

    %%%%%%%%%%%%%%%% file output
    fid = fopen(OUTname,'a');
    ti=toc;
    fprintf(fid,['ID: ',num2str(id),' Simulation done_____________________________\r']);
    fprintf(fid,[' Simulation time: ',num2str(num2str(ti)),'s, (', num2str(ti/60),\..
\..'min), (', num2str(ti/3600),'h)', ' Determining observables...\r']);
    fclose(fid);

   %%%%%%%%%%%%%%% Find observables
```

```
    tic
    % Occupation
    navg_RAW(:,:)=navg_RAW(:,:)+1./(Nruns)*sum(MCout,3);

    % fluctuations
    tempavgL=( sum(MCout.^2,1)/L );
    kavgL_RAW= kavgL_RAW+1/(Nruns)*sum( tempavgL ,3);
    kavgL_err_RAW= kavgL_err_RAW+1/(Nruns)*sum( tempavgL.^2 ,3);

    if (coll_rho=='1')
        % Density matrix elements
        for occ=0:Nmax
            for time=1:length(T)
                indices1=find(MCout(:,time,:)==occ);
                PnavgL_RAW(time,occ+1)=PnavgL_RAW(time,occ+1)+length(indices1)/(L*Nruns);
            end
        end
    end

    % Density Correlations
    for d=1:dmax;
        denstemp=sum(MCout(1:L,:,:).*MCout(mod((1:L)+d-1,L)+1,:,:),1)/L;
        densavgL_RAW(:,d)=densavgL_RAW(:,d)+1/Nruns*sum( denstemp ,3 )';
        densavgL_err_RAW(:,d)=densavgL_err_RAW(:,d)+1/Nruns*sum( denstemp.^2 ,3 )';
    end

%%%%%%%%%%%%%% file output
fid = fopen(OUTname,'a');
fprintf(fid,['ID: ',num2str(id),' Done____________________________\r']);
ti=toc;
fprintf(fid,['Elapsed time computing observables: ',num2str(ti),'s,\..
\.. (', num2str(ti/60),'min), (', num2str(ti/3600),'h)\r']);
fprintf(fid,['L=',num2str(L),', f=',num2str(f),', U=',num2str(U),', Gamma=',num2str(Gamma),\..
\..', J=',num2str(J),', taui=',num2str(taui),', tauf=',num2str(tauf),\..
\..', Runs=',num2str(Runs),'\r\r']);
fclose(fid);

%%%%%%%%%%%%%% Save data
clear('MCout','W','WL','WR','C','n','q','qnext','qR','qRp1','qL','qLm1','j',\..
\..'value','high','low','flag', 'Tlast','newseed','factor','c','OUTname','ti','run')
save([cdir,'/',name,'/RAW',num2str(id)])

end
```

Collecting the data, shell script:

```
#!/bin/bash
#$ -S /bin/bash
#$ -cwd

count=0
for file in RAW* ; do
```

```
let "count+=1"
done

Num_files=$count
echo "$count files found"

export OMP_NUM_THREADS=1

./colldataV12_1_run.sh $HOME/MCR/v713 $Num_files
```

Collecting the data, main code:

```
function coldataV12_3(Num_files_Total)
%%%%%%%%%%%%%%%%%%%%%%%%%%%%%%%%%%%%%%%%%%%%%%%%%%%%%%%%%%%%%%%%%%%%%%%%
% Function to collect data from MainMCV12_3
% Can collect data of several simuations, which can contain a different number of runs
% Input:
% - Num_files_Total: Total number of data files, counted in the shell script
% Output:
% - .mat file with all the observables
%%%%%%%%%%%%%%%%%%%%%%%%%%%%%%%%%%%%%%%%%%%%%%%%%%%%%%%%%%%%%%%%%%%%%%%%

%%%_____________________________ Convert input parameter to number
Num_files_Total=str2num(Num_files_Total);

%%%_____________________________ Determine the total number of runs in the data
Nruns_Total=0;
disp(['Loading data files to determine total number of runs...'])

for file=1:Num_files_Total
name=(['RAW',num2str(file)]);
load(name);
Nruns_Total=Nruns_Total+Runs;
end

disp(['Total number of runs: ',num2str(Nruns_Total)])

%%%_____________________________ Initializations
navg=zeros(L,Tpoints);                          % Avg. n over runs
kavgL=zeros(1,Tpoints);
kavgL_err=zeros(1,Tpoints);
densavgL=zeros(Tpoints,dmax);
densavgL_err=zeros(Tpoints,dmax);
if (coll_rho=='1')
    PnavgL=zeros(Tpoints,Nmax+1);        % Density matrix averaged over sites
end

tic
%%%_____________________________ Main loop to collect data
for file=1:Num_files_Total

%%%_______________ Load data
```

```
disp(['Loading data, file ',num2str(file),'/',num2str(Num_files_Total)])
name=(['RAW',num2str(file)]);
load(name);

%%%_____________ Determine compensation factor and observables
Compfact=Nruns/(Nruns_Total); %Compensation factor, needed if there are more files\..
\.. than initially calculated for
disp(['Compensation factor: ',num2str(Compfact)])
disp('Determining observables...')

    % Occupation
navg(:,:)=navg(:,:)+navg_RAW(:,:)*Compfact;

% fluctuations
kavgL= kavgL+kavgL_RAW*Compfact;
kavgL_err= kavgL_err+kavgL_err_RAW*Compfact;

% Density matrix elements
if (coll_rho=='1')
PnavgL=PnavgL+PnavgL_RAW*Compfact;
end

% Density Correlation
densavgL=densavgL+densavgL_RAW*Compfact;
densavgL_err=densavgL_err+densavgL_err_RAW*Compfact;

end

%%%____________ Estimate error, substract relevant quantities to obtain final observables
% fluctuations
kavgL_err=sqrt( (kavgL_err-kavgL.^2)/(Nruns_Total-1) );
kavgL=kavgL-f.^2;

% Density Correlation
densavgL_err=sqrt( (densavgL_err-densavgL.^2)/(Nruns_Total-1) );
densavgL=densavgL-f^2;

%%%__________________________ Save data
disp('Saving...')
clear('MCout')
name=(['L',num2str(L),'f',num2str(f),'U',num2str(U),'Gamma',num2str(Gamma),'J',\..
\..num2str(J),'tauf',num2str(tauf),'Nruns',num2str(Nruns_Total)]);
if (coll_rho=='1')
   name=([name,'_rho_']);
end
name=([name,'RES.mat']);
save(name);
disp('Done')
toc
end
```

Bibliography

[1] H. Pichler, J. Schachenmayer, A. J. Daley and P. Zoller, *Heating dynamics of bosonic atoms in a noisy optical lattice*, arXiv:1301.2803 (Jan. 2013)

[2] S. Trotzky, L. Pollet, F. Gerbier, U. Schnorrberger, I. Bloch, N.V. Prokof'ev, B. Svistunov, M. Troyer, *Suppression of the critical temperature for superfluidity near the Mott transition: validating a quantum simulator*, Nature Phys. 6, 998-1004 (2010)

[3] H. Pichler, A. J. Daley and P. Zoller, *Non-equilibrium dynamics of bosonic atoms in optical lattices: Decoherence of many-body states due to spontaneous emission*, Phys. Rev. A **82**, 063605 (2010)

[4] D. Poletti, J-S. Bernier, A. Georges and C. Kollath, *Dissipative quantum systems: from two to many atoms*, arXiv:1212.4254 (18 dec 2012)

[5] D. Poletti, J-S. Bernier, A. Georges and C. Kollath, *Interaction-induced impeding of decoherence and anomalous diffusion*, Phys. Rev. Lett. **109**, 045302 (2012)

[6] D. Poletti, P. Barmettler, A. Georges and C. Kollath, *Emergence of glass-like dynamics for dissipative and strongly interacting bosons*, arXiv:1212.4637 (Dec. 2012)

[7] M. H. Anderson, J. R. Ensher, M. R. Matthews, C. E. Wieman, E. A. Cornell, *Observation of Bose-Einstein Condensation in a Dilute Atomic Vapor*, Science 269, 198 (1995).

[8] K. B. Davis, M. -O. Mewes, M. R. Andrews, N. J. van Druten, D. S. Durfee, D. M. Kurn, and W. Ketterle, *Bose-Einstein Condensation in a Gas of Sodium Atoms*, Phys. Rev. Lett. 75, 3969-3973 (1995)

[9] Christopher J. J. Foot, *Atomic Physics*, Oxford University Press, 2005

[10] C.J. Pethick and H. Smith, *Bose-Einstein condensation in Dilute Gases*, Cambridge University Press, 2002

[11] I. Bloch, J. Dalibard and W. Zwerger, *Many-Body physics with ultracold gases*, Reviews of modern physics, Vol 80, July-September 2008

[12] N. W. Ashcroft and N. D. Mermin, *Solid State Physics*, Saunders College, 1976

[13] D. Jaksch, *BEC and optical lattices* Lecture notes, University of Oxford, UK

[14] M. P. A. Fisher, P. B. Weichmann, G. Grinstein and D. S. Fisher, *Boson localization and the superfluid-insulator transition*, Phys. Rev. B **40**, 546-570 (1989)

[15] M. Greiner, O. Mandel, T. Esslinger, T.W. Hänsch, and I. Bloch, *Quantum Phase Transition from a Superfluid to a Mott Insulator in a Gas of Ultracold Atoms* , Nature 415, 39-44 (2002)

[16] H.-P. Breuer and F. Pettruccione, *The theory of open quantum systems*, Oxford university press 2002

[17] H. Carmichael, *An open Systems approach to quantum optics*, Springer-Verlag 1991

[18] F. Gerbier and Y. Castin, *Heating rates for an atom in a far-detuned optical lattice*, Phys. Rev. A. **82**, 013615 (2010)

[19] K. Saito and Y. Kayanuma, *Nonadiabatic transition probabilities in the presence of strong dissipation at an avoided-level crossing point*, Phys. Rev. A **65**, 033407 (2002)

[20] J. J. García-Ripoll et al., *Dissipation-induced hard-core boson gas in an optical lattice*, New Journal of Physics **11**, 013053 (2009)

[21] J.-S. Bernier, Peter Barmettler, Dario Poletti and Corinna Kollath, *Emergence of long distance pair coherence through incoherent local environmental coupling*, arXiv:1211.4087

[22] C. W. Gardiner, *Handbook of Stochastic Methods for Physics, Chemistry and the Natural Sciences*, Springer-Verlag 1994

[23] H. Gould, J. Tobochnik and W. Christian, *An Introduction to Computer Simulation Methods: Applications to Physical Systems*, Addison-Wesley 2006

[24] All MF decoupled data are courtesy of Dario Poletti (Singapore University of Technology and Design, 20 Dover Drive, 138682 Singapore) and Bruno Sciolla (Département de Physique Théorique, Université de Genève, CH-1211 Genève, Switzerland)

[25] Werner Krauth, *Statistical Mechanics: Algorithms and Computations*, Oxford University Press

[26] Santiago A. Serebrinsky, *Physical time scale in kinetic Monte Carlo simulations of continuous-time Markov chains*, Phys. rev. E **83**, 037701 (2011)

[27] R.Eckhardt, *Stan Ulam, John von Neuman, and the Monte Carlo method*, Los Alamos Science, No 15, 1987

[28] H-P Breuer, W. Huber and F. Petruccione, *Fast nonequilibriums Monte Carlo simulation*

[29] A. F. Voter, *Introduction to the Kinetic Monte Carlo method*

[30] T.P.Schulze, *Kinetic Monte Carlo simulations with minimalsearching*, Phys. rev. E, **83**, 036704

[31] M.Abranowitz and I. A. Stegun, *Handbook of mathematical functions with Formulas, Graphs, and Mathematical Tables*, New York: Dover Publications, USA, 1960

[32] These plots may tend to be misleading since hops can happen at very short intervals. As a result, the plot sometimes shows a superposition of two system states, which aren't separated enough in time to be distinguished. In run (c) for example at $3.5 \cdot 10^{-5}$ three particle hops are shown at the same time: a hop from site 5 to 6, a hop form site 1 to 10 and a hop from site 5 to 6 (displacing an 'x' from site 6 to 5).